Mechanical Systems and Signal Processing 129 (2019) 337–365

Contents lists available at ScienceDirect

Mechanical Systems and Signal Processing

journal homepage: www.elsevier.com/locate/ymssp

A multidisciplinary approach to calibrating advanced numerical simulations of masonry arch bridges

Álvaro Bautista-De Castro [a], Luis Javier Sánchez-Aparicio [a,*], Pedro Carrasco-García [a], Luís F. Ramos [b], Diego González-Aguilera [a]

[a] Department of Cartographic and Land Engineering, University of Salamanca, High Polytechnic School of Ávila, Hornos Caleros, 50, 05003 Ávila, Spain
[b] ISISE, Department of Civil Engineering, University of Minho, Campus de Azurém, 4800-058 Guimarães, Portugal

ARTICLE INFO

Article history:
Received 27 April 2018
Received in revised form 20 February 2019
Accepted 16 April 2019

Keywords:
Masonry arch bridges
Geomatic techniques
Geophysical techniques
Ambient vibration tests
Sonic testing
Finite element model updating

ABSTRACT

This paper proposes a robust multidisciplinary method that combines geomatic procedures (terrestrial laser scanning and reverse engineering), geophysical methods (ground-penetrating radar and multichannel analysis of surface waves), sonic and impact echo tests, and ambient vibration approaches to generate accurate numerical simulations of masonry arch bridges. These methods are complemented by a robust finite element model updating method based on metamodeling global sensitivity analysis and a robust calibration strategy. The results obtained corroborate the feasibility of the proposed methodology with an average relative error in frequencies of 1.21% and an average modal assurance criterion of 0.93.

1. Introduction

Throughout history, masonry arch bridges have been one of the most frequently used constructions in transportation networks. These structures allow overpass of topographic features (such as gullies or rivers) and enable communication and trade between different places. Many of these masonry arch bridges, which were erected during the Roman and Mediaeval periods, are still in use and support new traffic demands for which accurate numerical simulations are necessary [1].

On this topic, accurate structural evaluation of a masonry arch bridge requires extensive knowledge of the different materials and structural systems presented. Within this context, several authors proposed the use of multidisciplinary approaches, with the aim of characterizing the bridge at different levels as follows [1–3]: (i) the geometrical level, (ii) the structural level, and (iii) the material level.

With respect to geometry, certain of these ancient constructions present complex and irregular shapes characterized by a succession of vaults and piers for which photogrammetry and terrestrial laser scanning have been the most suitable solutions [1,2,4]. The product of these procedures, the so-called point cloud, is subsequently used to extract sections or individual measurements for creation of CAD models that do not exploit the advantages offered by the latest advances in reverse engineering [5]. These procedures are able to mimic non-parametric shapes (e.g., existing deformations) using b-spline methods and non-uniform b-spline approaches. Moreover, this type of bridge presents a complex inner composition for which

* Corresponding author.
E-mail addresses: alvarobautistadecastro@usal.es (Á. Bautista-De Castro), luisj@usal.es (L.J. Sánchez-Aparicio), Retep81@usal.es (P. Carrasco-García), lramos@civil.uminho.pt (L.F. Ramos), daguilera@usal.es (D. González-Aguilera).

https://doi.org/10.1016/j.ymssp.2019.04.043
0888-3270/

ground-penetrating radar has been considered the most appropriate solution for characterization, allowing estimates of the thicknesses of spandrel walls, barrel vaults and layering of infill materials.

With respect to material characterization, two main structural components are noted in a masonry arch bridge: (i) masonry and (ii) infill. Masonry is used in the construction of vaults, piers and spandrel walls and can be characterized in situ using sonic tests [1]. These tests allow extraction of the Young's modulus and the Poisson's coefficient via analysis of the waves generated after excitation of the material [6,7]. Infill allows stabilization of the vaults and appropriate transmission of loads from the pavements, and its mechanical and physical properties are a critical issue in structural stability of masonry arch bridges [1,8–10]. Moreover, accurate characterization of the mechanical and physical properties of infill materials is complex, necessitating the use of invasive techniques to extract samples as well as another invasive methods (e.g., Ménard pressuremeter tests) used to locally obtain the infill parameters.

With respect to the structural characterization, many authors propose the use of ambient vibration tests as the most suitable strategy for evaluation of the global behaviour of historical structures [5,11,12]. It is especially useful if numerical simulation of the bridge is conducted using the finite element method, which allows the use of updating methods that enhance the accuracy of the model [1,5]. In these updating strategies, sensitivity approaches are required for evaluation of the influence of each variable in the dynamic response of the bridge. However, the large computational cost of each numerical simulation required in sensitivity analysis leads to the use of a low number of simulations to evaluate the sensitivity of each input via sensitivity methods based on the linear Spearman correlation matrix [5] or basic sensitivity analysis [1,13]. This complexity makes impossible the use of advanced and robust sensitivity methods such as the Sobol's indices [14]. These indices require the use of Monte Carlo simulations to obtain reliable results involving thousands of simulations [15].

Based on this foundation, this article proposes a new fully non-invasive multidisciplinary method that is able to overcome a subset of the main limitations in structural evaluation of historical masonry arch bridges. To this end, the proposed method uses the terrestrial laser scanner, ground-penetrating radar, the impact echo method, and reverse engineering procedures to create as-built CAD models that are able to depict the deformations presented in this type of structure. Moreover, the proposed approach also applies sonic tests for mechanical characterization of the masonry elements, the multichannel analysis of surface waves method for mechanical and physical characterization of infill (without the need for invasive techniques), ambient vibration tests for characterization of the global behaviour of the structure, and the finite element method for advanced numerical simulation of the bridge. Concerning the latter item, the finite element model is enhanced with the use of a robust updating method based on the polynomial chaos expansion meta-modelling strategy for evaluation of the Sobol's indices and the use of a non-linear least squares procedure to minimize the discrepancies between numerical and experimental data.

This methodology is specifically applied to a real case study, the Arco masonry arch bridge, which was erected over the Alberche river and is located in the Avila region of Spain. This ancient construction dates back to the XVIth century according to the description detailed by [16] and was later modified at the beginning of the XXth century to withstand current traffic loads. Thus, this construction presents two different infills, which require accurate mechanical and physical characterization.

This paper is organized as follows. After the Introduction, Section 2 presents the Arco Bridge, followed by Section 3, which describes the experimental campaign performed on this historical construction. Section 4 details the updating process of the numerical model, and finally, Section 5 presents the conclusions.

2. The Arco Bridge (Ávila, Spain)

2.1. Historical background

This historical masonry arch bridge is located on road AV-901, which connects the municipalities of Burgohondo and Villanueva de Avila in the southeast region of Castile and León in Spain. Erected over the Alberche river, this bridge has an origin believed to date back to the 16th century, according to its constructive characteristics [16]: (i) an eurhythmic design, (ii) the use of barrel vaults, (iii) the presence of regular masonry and (iv) a road without variation in width. Throughout its existence, this bridge has experienced modifications due to restoration work after its construction. On 2 October 1920, the rights to construction of a road connecting Avila with the municipality of Casavieja were granted to engineer D. Juan Manuel Torregrosa under a timeframe of completion on 31 March 1923, with this bridge as a component of this road. During this work, the original cambered road of the bridge was removed, a new layer of infill material was added, the spandrel walls were expanded, and the original parapets were replaced by others with larger width (Fig. 1a). However, due to bad weather in this location at the time of the work, the execution time was extended by eight months by order of the Directorate General of Public Works, with completion on 30 November 1923.

Of all of the information supplied on the restoration work performed on this historical construction, it is unknown when the wing wall (Fig. 1b) and the reinforced concrete on the pier (Fig. 1c) were added. However, according to the construction plans of the restoration work finished in 1923, it is known that both components were added after this rehabilitation project (Fig. 1a).

Finally, in 2010, the section of road AV-901 from Burgohondo to Villanueva de Avila was widened, with the exception of the bridge, and the drainage was rehabilitated. As a result, a layer of asphalt was added over the pavement of the bridge without replacement of its parapets.

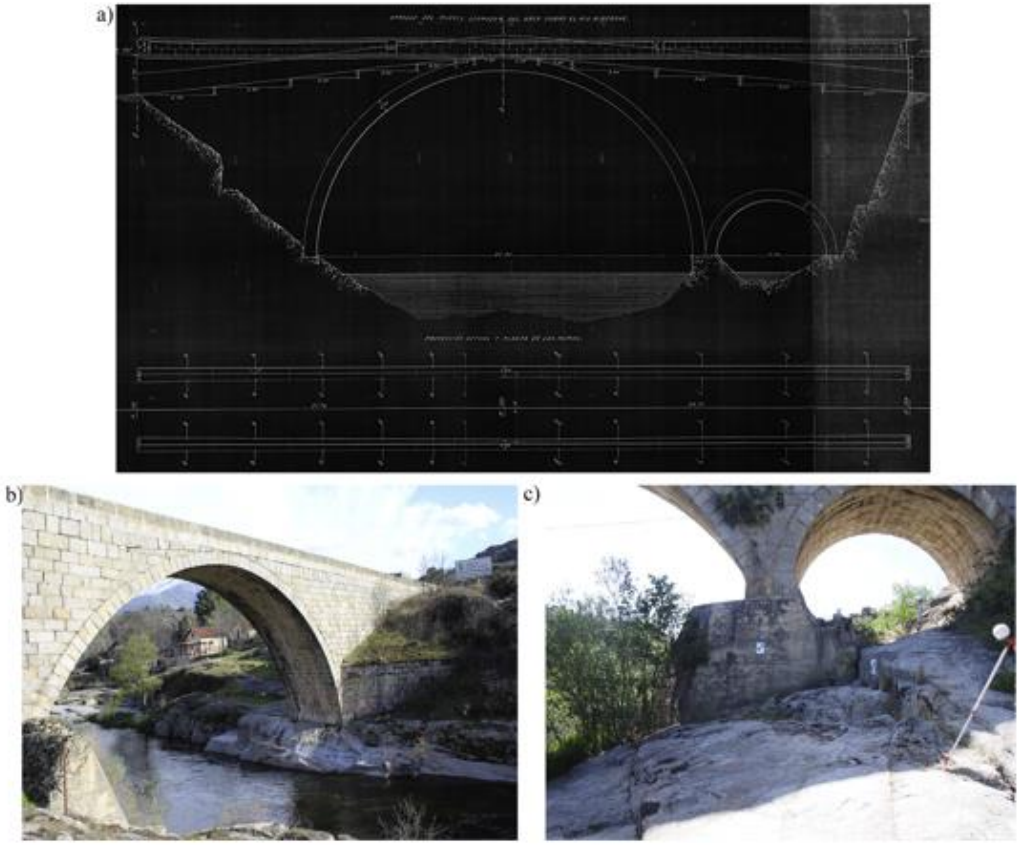

Fig. 1. The Arco Bridge: a) downstream elevation before and after restoration works; b) upstream elevation and; c) reinforced concrete layer added to the pier between vaults.

2.2. Description of the ancient masonry arch bridge

This historical construction presents a total length of approximately 45.91 m, and it contains the following structural components according to the existing drawings (Fig. 2): (i) a main barrel vault with a span of 22.20 m, a rise of 9.05 m and an average thickness of 0.70 m; (ii) a secondary barrel vault with a span of 6.60 m, a rise of 3.15 m and an average thickness of 0.60 m; (iii) spandrel walls with an average thickness of 0.60 m; (iv) a wing wall added after the rehabilitation work of 1923; and (v) a reinforced concrete pier between the two barrel vaults with a height of 4 m. With respect to its inner geometry, the bridge contains the following components: (i) an original infill layer with a maximum depth of 7.11 m, and (ii) an added layer of infill material from the rehabilitation work of 1923 with maximum heights of 2.14 m and 2.30 m at the ends of the bridge.

Complementary to this information, the non-structural elements of the bridge include the following (Fig. 2): (i) asphalt pavement with 150 mm thickness and (ii) two parapets with a height and width of 1000 mm and 400 mm, respectively.

2.3. Damage identification on the bridge: visual inspection

Prior to the experimental campaign on the bridge, visual inspection was conducted to assess its current state and verify the presence of different types of visual indicators of damage (Figs. 3 and 4): (i) out-of-plane deformations and cracks in portions of the spandrel walls, (ii) soiling and white crusts on the barrel vaults due to salts from the mortar used to restore the barrel vaults, (iii) graffiti on the main barrel vault, the wing wall and a parapet, (iv) higher plants on the mortar joints of the spandrel walls and on the mortar joints between the barrel vaults and the spandrel walls, (v) lichens on the wing wall, and (vi) moss. The origin of certain of these damages, such as the out-of-plane deformations and masonry cracks, appear to be related to the current demands of traffic loads as well as unexpected natural events that have occurred in the past.

In addition to the damage indicators previously shown, it was possible to detect two type of masonry (Fig. 4): (i) masonry with material losses in its joints in the spandrel walls and (ii) a masonry without material losses in its joints in the barrel vaults.

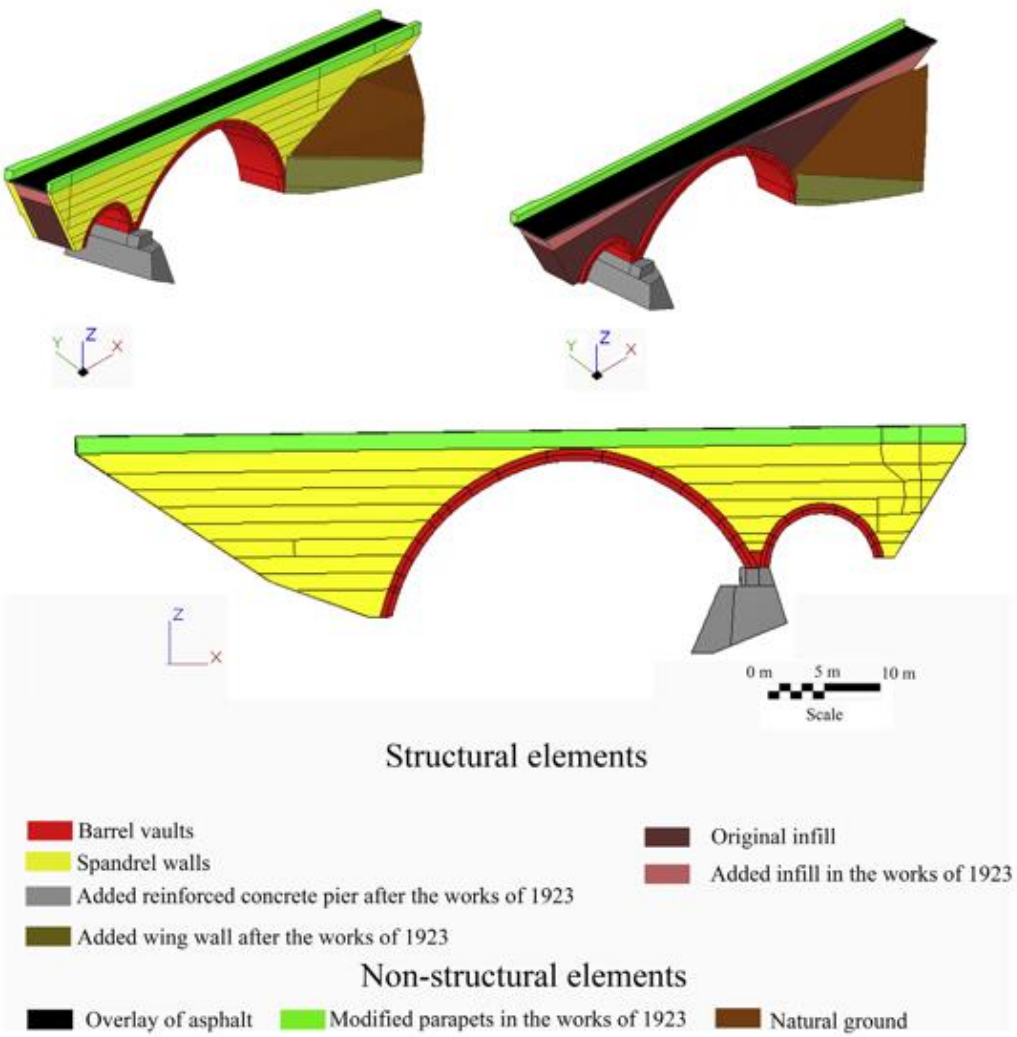

Fig. 2. Structural elements and non-structural elements of the Arco Bridge.

3. Experimental campaign: mechanical, geometrical and dynamical characterization of the Arco Bridge

Accurate numerical simulation of the bridge requires an extensive knowledge of the different structural components of the bridge, and therefore, the below workflow was conducted (Fig. 5).

3.1. Mechanical characterization of materials: multichannel analysis of the surface wave method and sonic tests

Built from masonry, the Arco Bridge is composed of grey granitic spandrel walls and grey granitic barrel vaults originating from the local quarries of Avila. Concerning the inner composition of the structure, historical documentation (Section 2.1) revealed two layers of infill material (Fig. 2). According to this information and considering the relevance of an accurate characterization of the mechanical properties of these structural components, the following non-destructive techniques were used: (i) multichannel analysis of surface waves and (ii) sonic tests.

3.1.1. Multichannel analysis of surface waves

The infill of the bridge can be considered as a soil inserted within the space delimited by its spandrel walls and vaults. Therefore, geophysics can offer a solution for extraction of the mechanical and physical properties of the soils, namely, multichannel analysis of surface waves (MASW) [17,18]. This method allows extraction of the phase velocities and frequencies of the waves created after excitation of a soil. This excitation was performed using a 20.00 kg tenderizer connected to a data

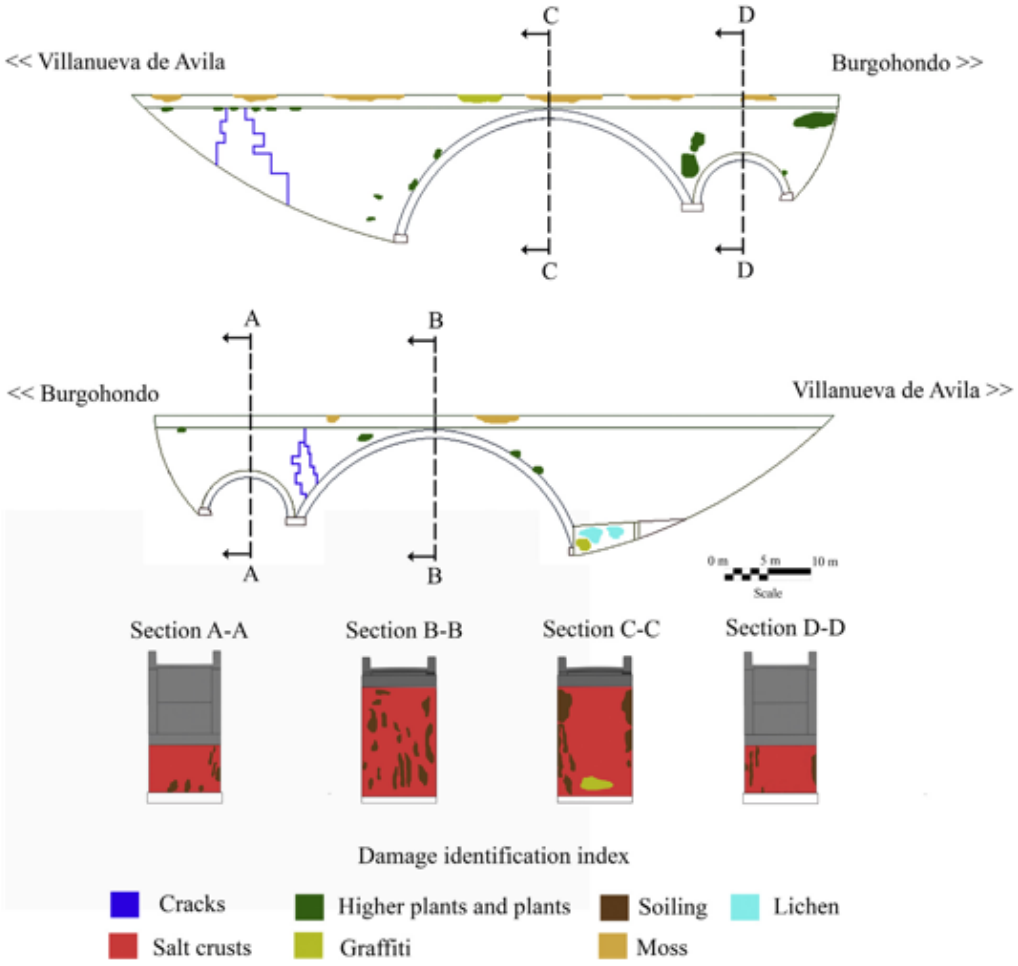

Fig. 3. Damage mapping performed during the visual inspection.

acquisition unit (Fig. 6), and data were captured through a linear array of 24 geophones with a natural frequency of 4.5 Hz. The sensors were placed along the asphalted pavement of the bridge separated by a distance of 0.5 m over a total length of 11.5 m (Fig. 7). To evaluate the reliability of the data acquired, a total of 4 setups were constructed (Fig. 7).

According to the constructive disposition of the bridge and the expected infill distribution (Fig. 2), four setups were installed (Fig. 7). Each setup consisted of a total of 24 geophones with a natural frequency of 4.5 Hz (Fig. 6b) placed along the asphalt pavement of the bridge, separated by a distance of 0.5 m over a total length of 11.5 m (Fig. 7).

From the excitation data captured by the geophones, it was possible to extract the dispersion curve of the soil and its principal model. An optimization procedure known as inversion analysis was performed to obtain the average shear-wave velocities of the soil (*Vs*) with respect to the depth (Fig. 8). Additionally, this method was able to record the primary wave speeds (*Vp*). [17]. The two speeds (*Vs* and *Vp*) are related to the Young's modulus, density, shear modulus and bulk modulus of the soil (Eqs. (1)–(4)).

$$\rho = 1.2475 + 0.399(V_p/1000) - 0.026(V_p/1000)^2 \tag{1}$$

$$E = \rho V_s^2 \frac{3\left(\frac{V_p}{V_s}\right)^2 - 4}{\left(\frac{V_p}{V_s}\right)^2 - 1} \tag{2}$$

$$G = \rho V_s^2 \tag{3}$$

Fig. 4. Current state of conservation of the bridge: a) cracks on the spandrel wall; b) Salt crusts and soiling on the smaller barrel vault; c) Salt crusts, soiling, and graffiti on the bigger barrel vault and d) higher plants on the spandrel wall.

$$K = \rho V_p^2 - \frac{4}{3}G \tag{4}$$

where ρ is the density in kg/m^3, E is the Youngś modulus in GPa, V_p is the primary wave speed of the soil in m/s, G is the shear modulus in GPa, K is the bulk modulus in GPa, and V_s is the shear-wave speed of the soil in m/s.

In addition to these mechanical properties, the N_{spt} (number of blows from the standard penetration tests) of the soil is obtained using Eq. (5).

$$V_s = 85.35N_{spt}^{0.348} \tag{5}$$

As a result, it is possible to characterize the infills of the bridge from a mechanical and physical point of view (Table 1) and estimate the average depths using the V_s obtained during the experimental campaign (Fig. 8).

The large values obtained for the upper bounds of the "original infill layer" (Table 1) can be explained by the presence of selected intrusions of natural soil within the space delimited by the spandrel walls (Figs. 1 and 2).

3.1.2. Sonic testing

In addition to the MASW tests, several indirect sonic tests were conducted in different locations on the bridge with the aim of characterizing the masonry from a mechanical point of view (Fig. 9).

During these tests, an instrumental hammer, a data acquisition unit with 24 bits of resolution and a maximum sampling rate of 100 kHz and several piezoelectric accelerometers (transducers) with a sensitivity of 10 V/g, range of ± 0.5 g and 8 μg rms broadband resolution were used. For each area evaluated, the material was excited with the instrumental hammer, and its excitation (in the form of compressional or primary waves (V_p) and surface or Rayleigh waves (V_r)) was recorded by the

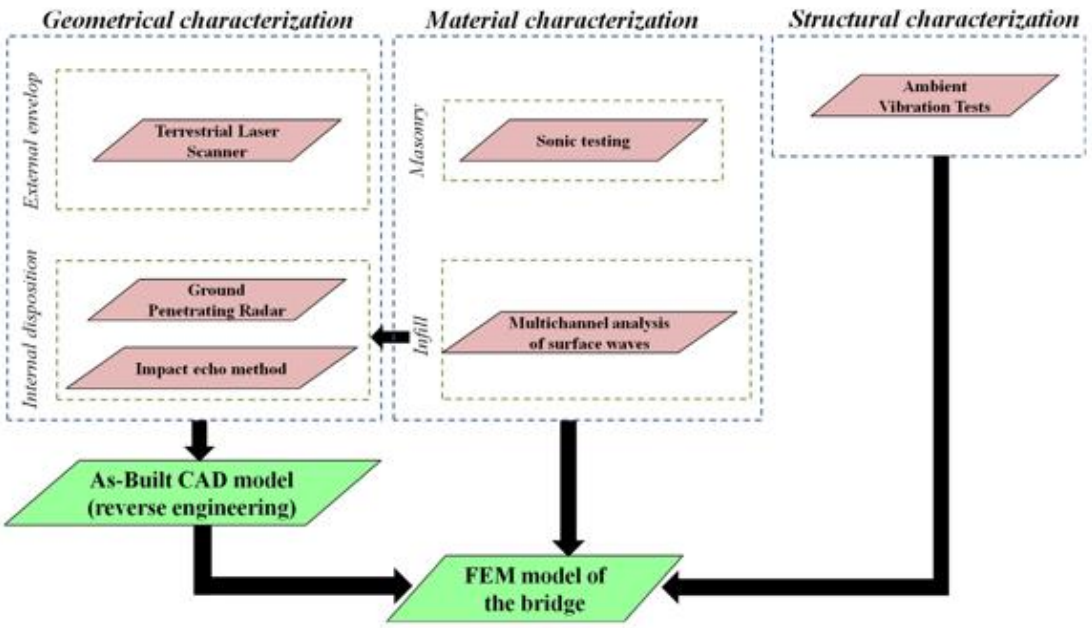

Fig. 5. Workflow of the proposed methodology.

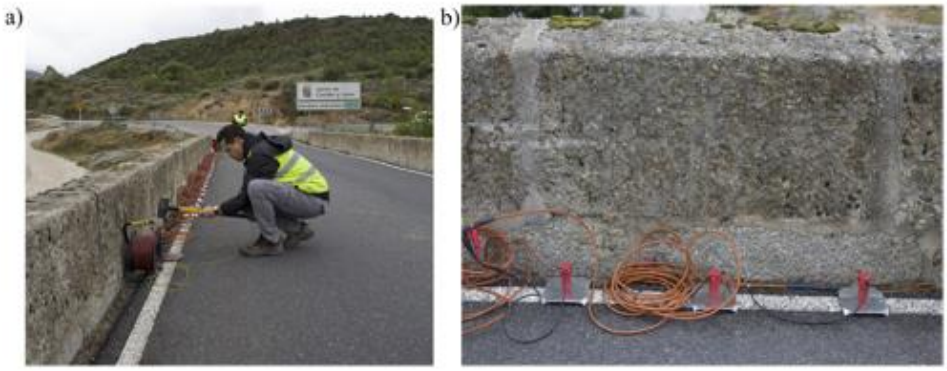

Fig. 6. MASW test carried out on the bridge: a) instrumental hammer and b) geophones with a natural frequency of 4.5 Hz.

transducers. The following equations were applied to evaluate the mechanical properties of the masonry: (Eqs. (6)–(8)) [6,19].

$$V_P = \left(\frac{E(1-\nu)}{\rho(1-\nu)(1-2\nu)}\right)^{1/2} \tag{6}$$

$$V_r = \frac{0.87+1.12\nu}{1+\nu}\left(\frac{E}{2\rho(1+\nu)}\right)^{1/2} \tag{7}$$

$$\frac{V_p}{V_r} = \frac{0.87+1.12\nu}{1+\nu}\left(\frac{(1-2\nu)}{2(1-\nu)}\right)^{1/2} \tag{8}$$

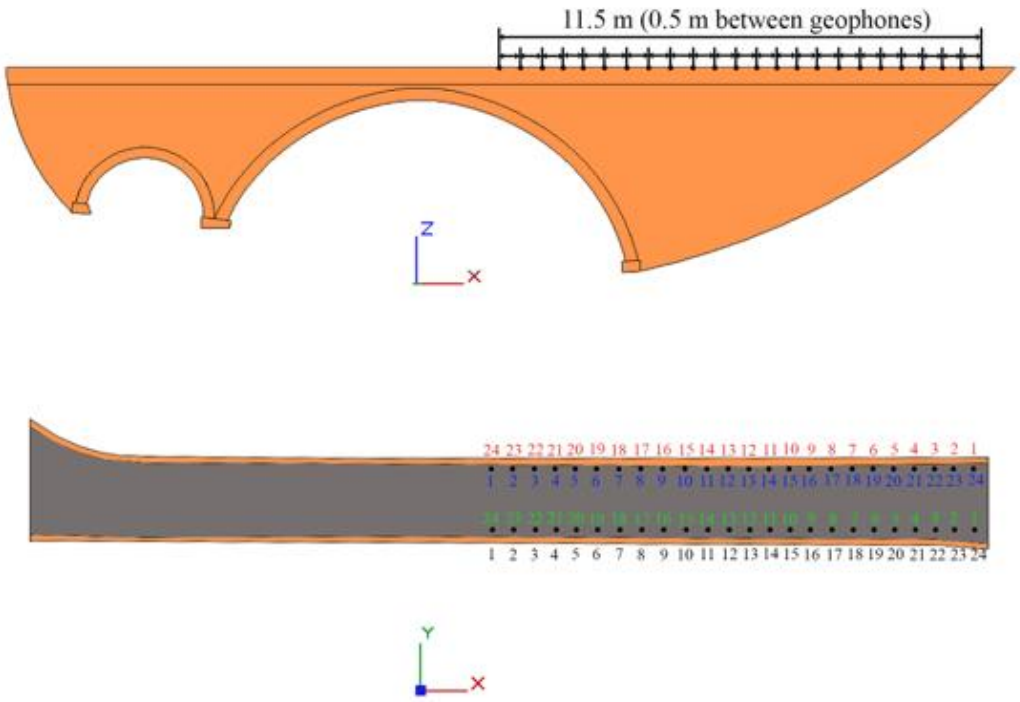

Position 1 of the 24 geophones

Setup 1: 1, 2, 3, 4, 5, 6, 7, 8, 9, 10, 11, 12, 13, 14, 15, 16, 17, 18, 19, 20, 21, 22, 23, 24

Setup 2: 1, 2, 3, 4, 5, 6, 7, 8, 9, 10, 11, 12, 13, 14, 15, 16, 17, 18, 19, 20, 21, 22, 23, 24

Position 2 of the 24 geophones

Setup 3: 1, 2, 3, 4, 5, 6, 7, 8, 9, 10, 11, 12, 13, 14, 15, 16, 17, 18, 19, 20, 21, 22, 23, 24

Setup 4: 1, 2, 3, 4, 5, 6, 7, 8, 9, 10, 11, 12, 13, 14, 15, 16, 17, 18, 19, 20, 21, 22, 23, 24

Fig. 7. Setups and geophones positions used during the mechanical characterization of the two infill layers.

According to the results supplied by the indirect sonic tests (Table 2), two different type of masonry can be considered: (i) the masonry of the spandrel walls, which shows an average Young's modulus of 1.79 GPa, and (ii) the masonry of the barrel vaults with an average Young's modulus of 3.28 GPa. These values are in agreement with the results obtained during the visual inspection (Section 2.3) and appear to be related to the conservation state of the joints because the stones evaluated via indirect tests presented similar velocities (Fig. 9 and Table 3).

3.2. External geometrical characterization: terrestrial laser scanning

Due to difficulty in accessing certain components of the bridge and the extension of the infrastructure, the use of a TLS is the best solution, given its flexibility and rapid data acquisition and processing. To this end, a lightweight TLS Faro Focus 3D 120® instrument was used to digitalize the entire structure. This laser scanner is based on the phase-shift physical principle [20], which applies a significant compromise between data acquisition rate and accuracy (Table 4).

As an addition to the TLS system, several registration spheres with two different diameters (20 cm and 14.5 cm) and several planar targets (Fig. 10b) were used with the purpose to automatically align the different scan stations. To this end, a target-based registration procedure was conducted.

As a consequence, 26 scan stations were needed to conduct 3D digitalization of the entire construction, and these scan stations were distributed as follows: (i) a total of 13 scans on the bridge deck and (ii) a total of 13 scans under the bridge. The alignment error resulting from these scans was 0.009 ± 0.008 m. Considering the goal of the point cloud and the creation of a suitable CAD model for further numerical simulations, additional procedures were required to simplify the large amount of data captured (62,689,274 points). To this end, the procedure proposed in [5] was used. From this process, a more sim-

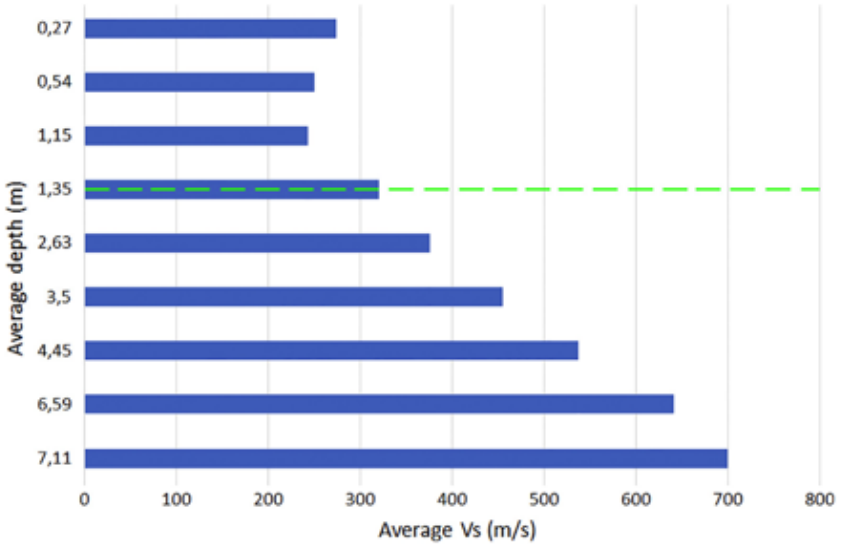

Fig. 8. Estimation of the infill layers through the relation between the average depths and the average V_s speeds. The green line represents the interface between the added and original infill layers.

Table 1
Upper bounds, lower bounds, average values and coefficients of variation (Cov) of the N-SPT, Young Modulus, shear modulus, bulk modulus, Poisson's ratio and density obtained from the MASW tests in the two infill materials. In brackets, the average depths of the added and original infill layers.

		Added infill layer (1.35 m)	Original infill layer (7.11 m)
N-SPT	Upper bound	57.29	581.97
	Lower bound	6.67	52.86
	Average value	29.37	283.54
	Cov (%)	51.02	60.61
Young Modulus (GPa)	Upper bound	0.78	3.18
	Lower bound	0.33	0.56
	Average value	0.41	1.73
	Cov (%)	24.46	41.01
Shear modulus (GPa)	Upper bound	0.19	0.96
	Lower bound	0.11	0.26
	Average value	0.14	0.60
	Cov (%)	34.54	41.85
Bulk modulus (GPa)	Upper bound	4.91	7.08
	Lower bound	3.90	4.88
	Average value	4.44	6.10
	Cov (%)	6.41	11.08
Poisson's ratio	Upper bound	0.50	0.48
	Lower bound	0.48	0.43
	Average value	0.49	0.46
	Cov (%)	0.90	3.02
Density (kg/m^3)	Upper bound	1847.00	1961.00
	Lower bound	1787.00	1848.00
	Average value	1819.00	1909.00
	Cov (%)	0.95	1.80

plified 3D representation of the bridge was obtained with a total of 18,233,172 points (29.08% of the points of the original point cloud) (Fig. 11).

3.3. Internal geometrical characterization: ground-penetrating radar and the impact echo method

3.3.1. Ground-penetrating radar

The ground-penetrating radar (GPR) technique was chosen to characterize the distribution of the inner composition of the bridge from a geometrical point of view as well as the thicknesses of the barrel vaults and spandrel walls. The equipment

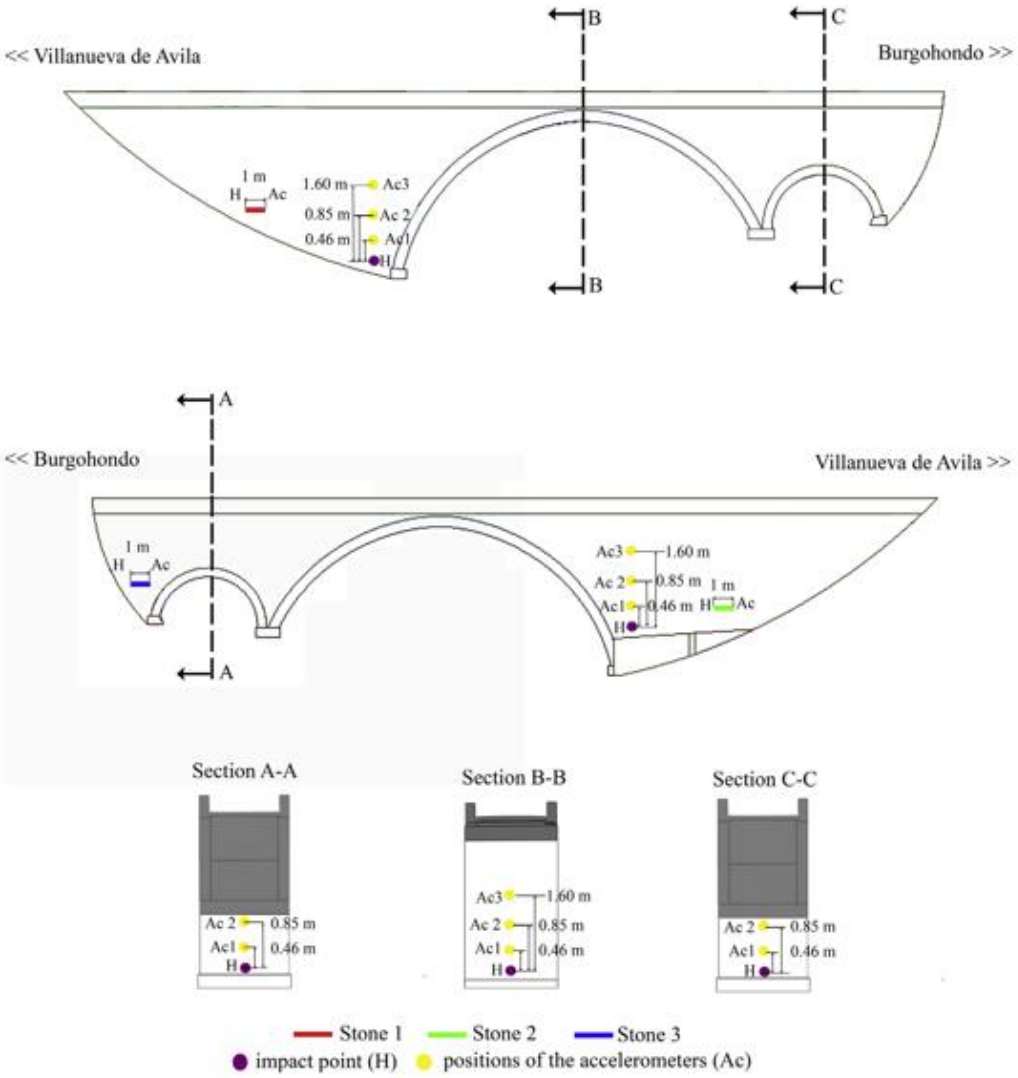

Fig. 9. Places considered for the indirect sonic testing.

Table 2
Results obtained from the indirect sonic tests carried out on the bridge. It is worth mentioning, that a range of densities between 2000 and 2500 kg/m^3, were considered with the aim of obtaining a confidence range of admissible values for the different mechanical properties.

	Spandrel walls		Barrel vaults	
	P-wave	R-wave	P-wave	R-wave
Average velocity (m/s)	1110.00	588.00	1240.00	657.00
Cov (%)	1.56	1.75	0.68	0.55
Poisson's coefficient	0.26		0.24	
Density (kg/m^3)	2000–2500		2000–2500	
Youngs modulus (GPa)	1.00–2.57		2.56–4.00	

applied for this purpose included a X3M® GPR system from MALA Geoscience, which was used to capture a total of six profiles (Fig. 12): (i) two longitudinal profiles in opposite directions to obtain additional information on the homogeneity and stratification of the infill materials, in addition to the thicknesses of the barrel vaults, with a central frequency of 250 MHz

Table 3
Results obtained from the indirect tests carried out on the stones.

	Stone 1		Stone 2		Stone 3	
	P-wave	R-wave	P-wave	R-wave	P-wave	R-wave
Average velocity (m/s)	1113.14	589.96	1146.56	607.68	1113.80	590.31
Cov (%)	0.10	0.08	1.12	1.08	0.06	0.04
Poisson's coefficient	0.26		0.26		0.26	
Density (kg/m^3)	2000–2500		2000–2500		2000–2500	
Young's modulus (GPa)	2.02–2.53		2.15–2.68		2.03–2.53	

Table 4
Technical specifications of the TLS Faro Focus 3D 120®.

Faro Focus 3D 120®	
Measurement principle	Phase shift
Wavelength	905 nm
Measurement range	0.6–120 m
Accuracy nominal value	2 mm to 25 m in normal conditions of illumination and reflectivity
Field of view	360° Horizontal 305° Vertical
Capture rate	122,000/976,000 points
Beam divergence	0.19 mrad

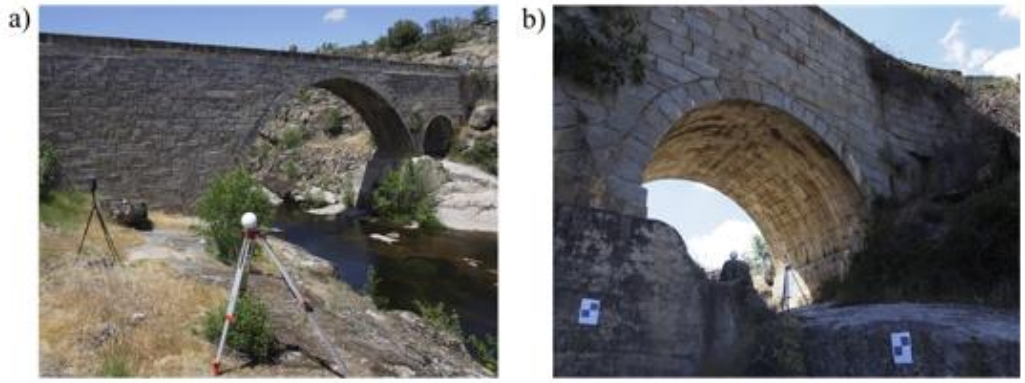

Fig. 10. TLS data acquisition: a) TLS Faro Focus 3D 120® and registration spheres used for scanning the bridge; b) registration spheres and planar targets at the lower part of the bridge.

and a total time-window of 28 ns; and (ii) four profiles in the vertical direction with the aim of characterizing the thickness of the spandrel walls with a central frequency of 800 MHz and a total time-window of 104 ns.

Each horizontal profile (Figs. 12c and 13a) was used to identify two different infill layers (Fig. 2) through the reflection produced between its interfaces until a maximum of 42 ns (2.15 m), whereas the pavement (Fig. 2) was identified by the paving-infill interface at 2 ns (0.20 m). These measurements were obtained with a pre-calibrated velocity of 0.1 m/ns [21]. Moreover, these horizontal profiles were used to estimate the thicknesses of the barrel vaults at an average travel-time distance of 12 ns, corresponding to a thickness value of 0.70 m for the larger barrel vault, whereas the smaller barrel vault did not appear in the horizontal profiles (Fig. 13a) due to the limited depth of penetration of the system. For this reason, a thickness of 0.70 m was assumed for the smaller barrel vault according to the drawings of the bridge (Fig. 1a). Furthermore, the thickness measurement of the larger barrel vault was obtained by the time distance travelled between the reflections of the arch-air interface and the masonry-infill interface, with a pre-calibrated velocity of 0.1 m/ns for granitic ashlar [21]. It is worth mentioning that the thickness values of the asphalt and the major barrel vaults were compared with the data supplied by the most recent restoration project due to the amount of geometrical uncertainty obtained by the 250 MHz GPR antenna.

Additionally, the vertical profiles (Figs. 12a, b and 13b, c) were used to identify the thickness of the spandrel walls via the reflection produced in the masonry-infill interface due to the dielectric contrast between media and the reflections patterns of the infill. Therefore, with the difference between this reflection and the direct-wave reflection at the surface level (air-masonry interface), the thickness of the spandrel walls was estimated at 10 ns (0.60 m) with a pre-calibrated velocity of 0.13 m/ns [21].

Fig. 11. 3D representation of the optimized point cloud of the bridge.

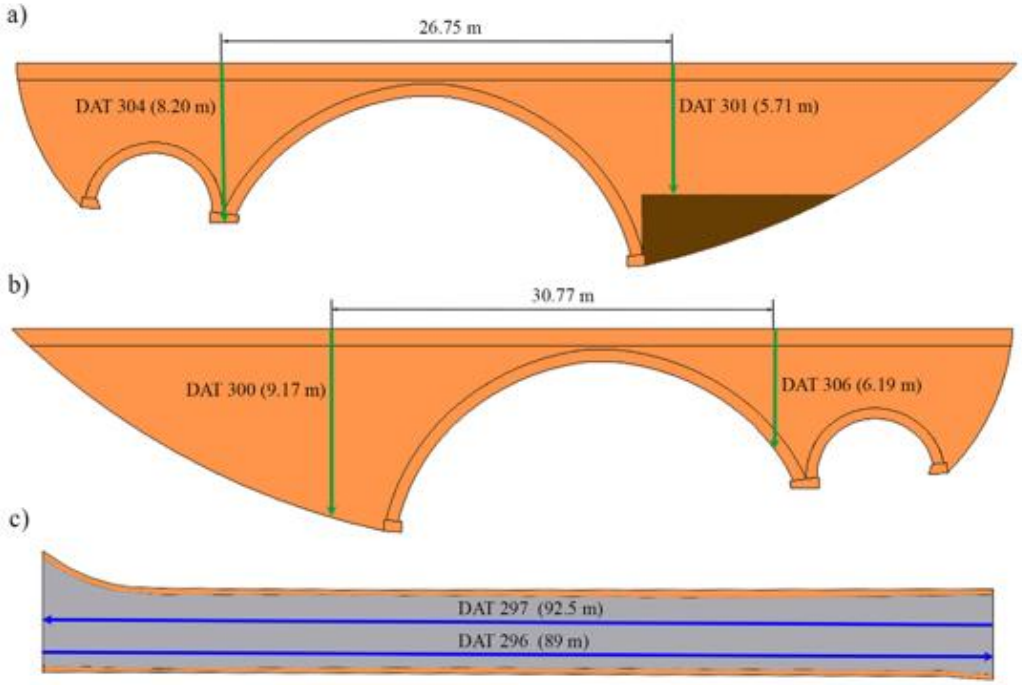

Fig. 12. Positions of the GPR tests considered to characterize the inner distribution of the bridge: a) upstream elevation; b) downstream elevation and; c) plant view. In green the vertical profiles and in blue the horizontal profiles.

It was also possible to observe a high amount of reflections in the area of the masonry, suggesting the presence of holes on the interface between the masonry and the infill as well as in the masonry joints, which was in accordance with the visual inspection and the mechanical values obtained during the sonic tests (Fig. 3 and Table 2).

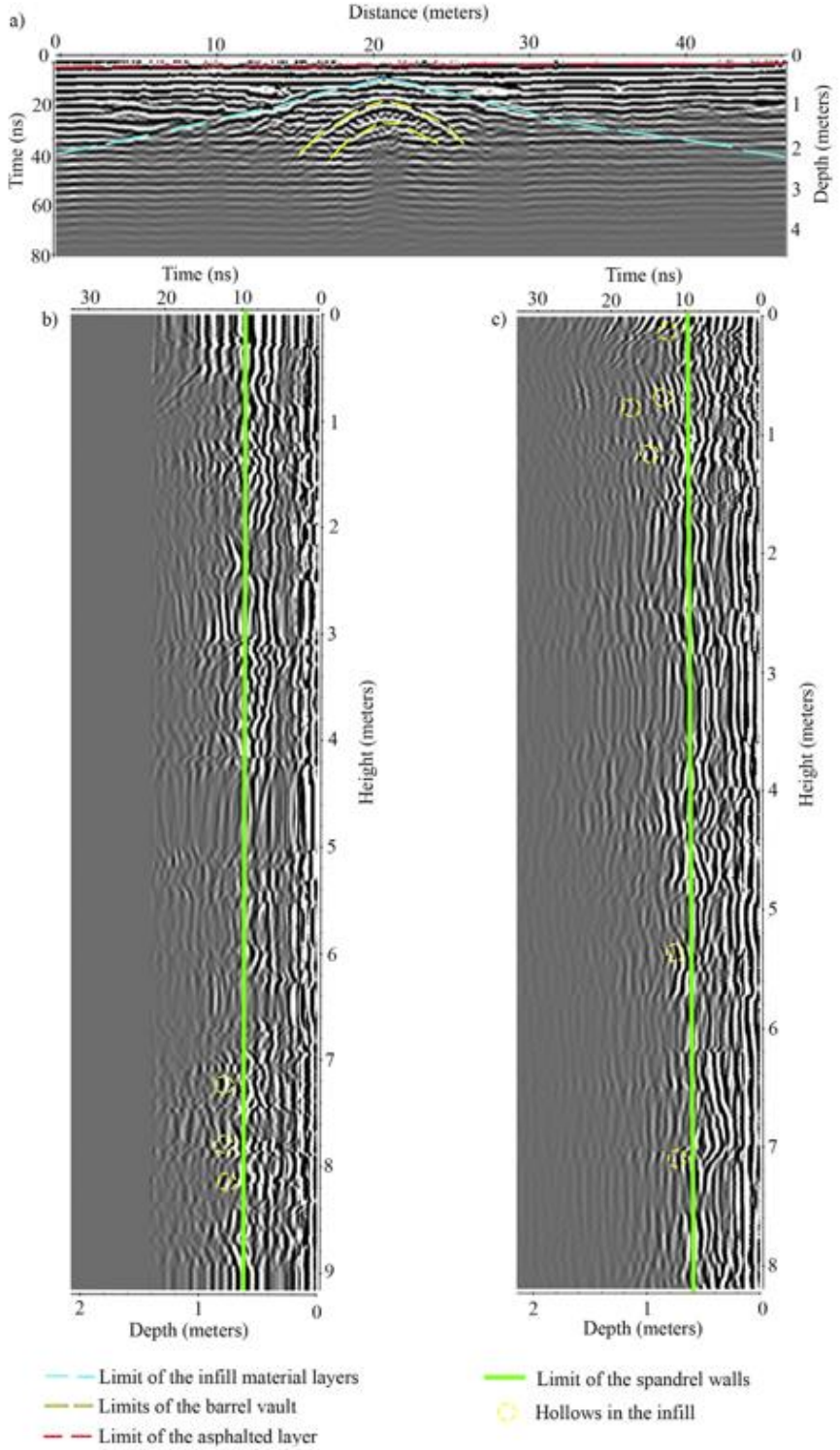

Fig. 13. Results obtained by the ground penetrating radar: a) asphalted layer, infill material layers and barrel vault thickness (DAT 296); b) and c) thickness of the spandrel walls and hollows in the infill layers (DAT 300 and DAT 304).

3.3.2. Impact echo method

The impact echo method was used to ensure and compare the thicknesses of the spandrel walls obtained from the vertical profiles by the GPR (Figs. 12a, b and 13b, c). This test was used to determine the changes in the inner composition of solids (e.g., cracks into elements made by concrete) via Fourier analysis of the wave generated during excitation of the material [22]. During these tests, the same instruments as those used in indirect sonic testing were applied. In this case, the instrumental hammer and the transducers were placed in the same positions (Fig. 14a) considering the starting and ending point as the same point. The excitation captured by the transducer was later transformed into a frequency spectrum via the fast Fourier transform (FFT) (Fig. 14b). The peaks of this spectrum denote the presence of inhomogeneities inside the material and thus indicate the interfaces between the masonry and the infill.

According to this information, 3 impact echo tests were conducted at different points of the bridge (Fig. 9). To obtain reliable results, a total of 10 impacts were performed on each point. The FFT and Eq. (4) were used to obtain the thickness of the spandrel walls (Table 5). It is worth mentioning that this equation requires knowledge of the velocity of the material, using the velocity (V_p) of the stone obtained during sonic testing (Table 3).

$$V_P = 2df \tag{9}$$

where V_p is the velocity of the P-wave in m/s of the stone; d is the thickness of the material in m; and f corresponds to the frequency of the peak in Hz.

As a result, an average spandrel wall thickness of 0.59 m was obtained, with a difference of 1.67% with respect to the average spandrel wall thickness obtained by the GPR (0.60 m) (Table 5).

3.4. Dynamic identification: ambient vibration tests (AVT)

Based on the operational modal analysis (OMA) approach, a dynamic identification campaign was conducted to identify the dynamic properties of the masonry arch bridge: (i) frequencies, (ii) modal displacements and (iii) damping ratios. With the aim of obtaining better results, several numerical evaluations (eigenvalues analysis) were performed. In this context, the results obtained by the tests and the previously shown procedures were considered (CAD model and mechanical properties of the different structural components) as well as the different boundary conditions (with all degrees of freedom fixed and all degrees of freedom fixed except for the Y-axis translation). These previous dynamic simulations were used to establish the most suitable configuration for the OMA tests (such as acquisition time and sampling rate) in addition to placement of the accelerometers in the proper areas of the bridge.

Considering the results obtained from these previous simulations, three setups were used with an acquisition time of 20 min and a sampling rate of 256 Hz. For each setup, a total of 12 uniaxial piezoelectric accelerometers with a sensitivity of 10 V/g, range of ±0.5 g and 8 μg rms broadband resolution were placed along the bridge pavement. Of the 12 accelerometers used during the tests, 7 were considered as references (fixed positions) in the following directions (Fig. 15): (i) accelerometers (3), (4), (5) and (10) in the Z-direction and (ii) accelerometers (2), (4) and (6) in the Y-direction.

Finally, based on raw time series, the stochastic subspace identification principal component algorithm (SSI-PC) was used to determine the frequencies, damping ratios and modal shapes and to obtain the dynamic properties of the bridge [23]. As a result, a total of 5 modes were identified, with frequencies ranging from 5.56 Hz to 18.09 Hz (Table 6 and Fig. 16). The low coefficients of variation (Cov) for the frequencies and damping ratios revealed the quality of the obtained modal properties. For the damping ratio, an average value of 3.48% was obtained.

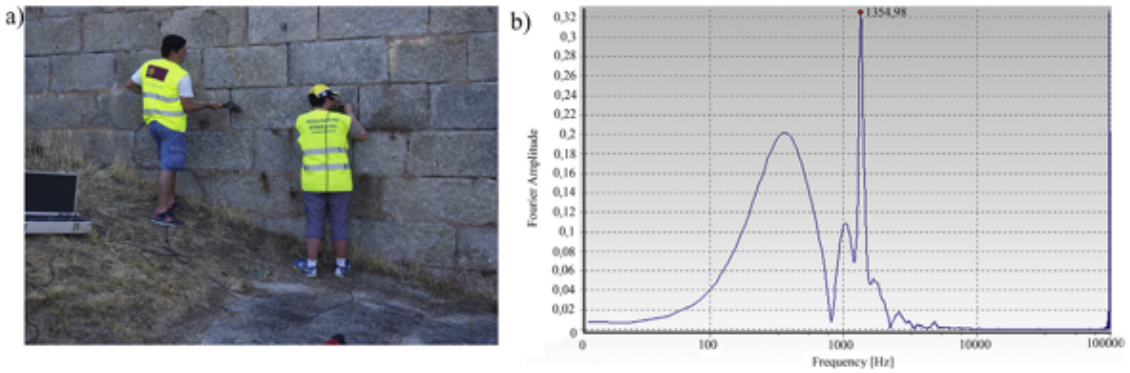

Fig. 14. Impact echo tests carried out on the bridge: a) instrumented hammer and accelerometer and; b) identified peak from the frequencies obtained by the Fourieŕs spectrum.

Table 5
Comparison between the spandrel walls thicknesses obtained by the impact echo tests regarding average spandrel walls thickness obtained by the GPR.

Number of stone	Average velocity of the P-waves (m/s)	Average frequency (Hz)	Thickness (m)	Average thickness (GPR)	Difference (%)
Stone 1	1113.14	915.53	0.61	0.60	1.67
Stone 2	1146.56	791.63	0.72	0.60	20.00
Stone 3	1113.80	1298.83	0.43	0.60	28.33

4. Numerical model of the current state of the bridge

Robust structural evaluation of masonry arch bridges requires the development of an extensive experimental campaign with the aim of characterizing the structure from different points of view and accurate design of numerical models able to reproduce the structural behaviour against different causes, such as static or seismic loads. In this sense, the use of the finite element method (FEM) is one of the most frequently used solutions for the structural evaluation of bridges [1,5,13].

4.1. From the point cloud to the numerical model

Considering all of the data supplied by the experimental campaign, an as-built CAD model was constructed. This CAD model was created with the external envelope from the TLS (Fig. 11) and the inner distribution of the different infills and thickness of the masonry from the GPR and impact-echo tests (Figs. 12 and 13) (Section 3.3.2).

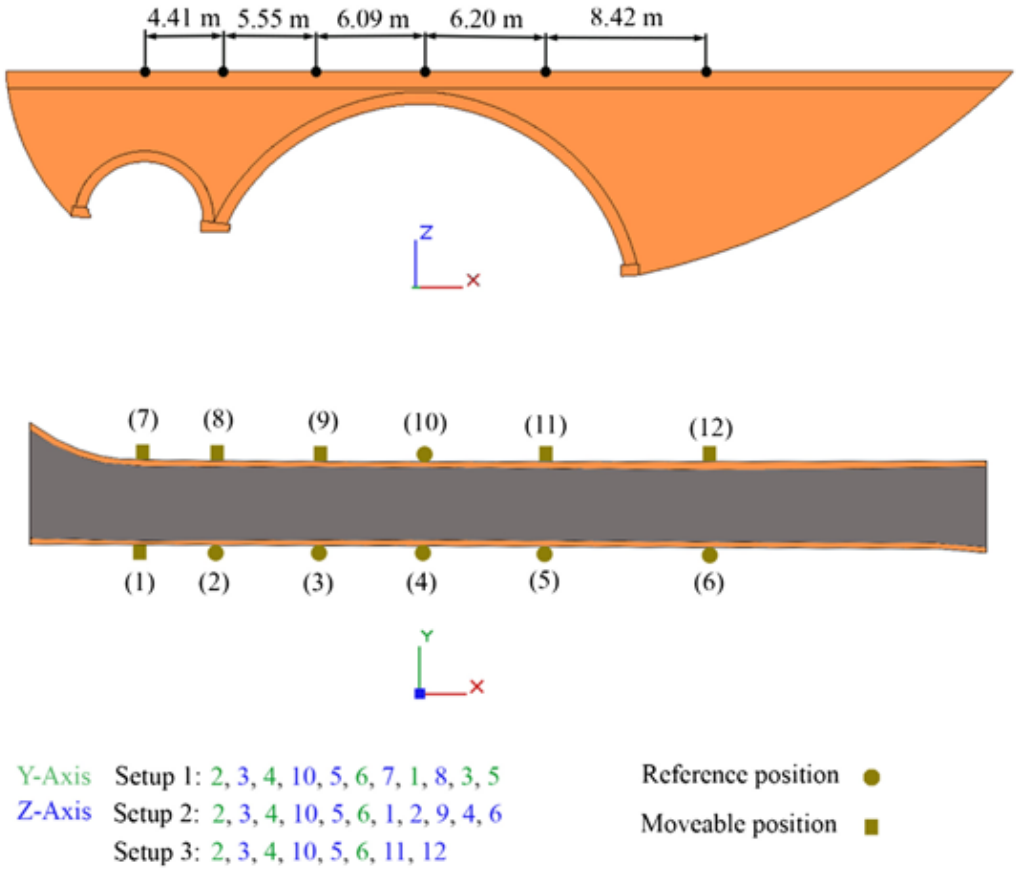

Fig. 15. Setups and positions of the accelerometers used during the dynamical identification campaign.

Table 6
Natural frequencies and damping ratios obtained from the AVT.

Mode shape	Frequencies (Hz)	CoV (%)	Damping ratios (%)	CoV (%)	Description
1	5.56	0.02	2.53	1.60	1st asymmetrical translational (Y-axis)
2	8.22	<0.01	2.29	2.50	2nd asymmetrical translational (Y-axis) 1st asymmetrical torsional (X-axis)
3	9.31	0.02	4.30	1.83	3rd asymmetrical translational (Y-axis) 1st asymmetrical vertical bending (Z-axis)
4	11.47	0.04	3.63	2.47	2nd asymmetrical vertical bending (Z-axis)
5	18.09	0.03	4.65	2.87	4th asymmetrical translational (Y-axis) 2nd asymmetrical torsional (X-axis)

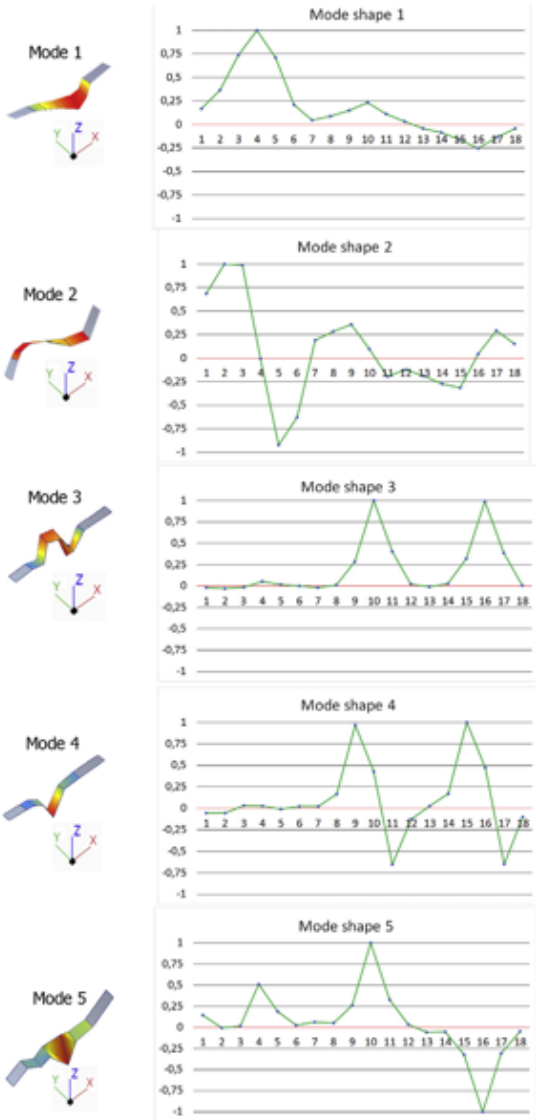

Fig. 16. Graphical representation of the vibrational modes obtained by the SSI-PC algorithm. The green line are the experimental modal displacements. The horizontal axis and the vertical axis of the graphs represent the degree of freedoms and the normalized modal displacements, respectively.

The as-built CAD model was analysed using the methodology defined by [5]. This methodology includes the following stages: (i) alignment of the point cloud according to the main axis of the bridge (Fig. 17) and (ii) construction of the CAD model via reverse engineering procedures.

For the first stage, principal component analysis was applied over the entire point cloud with the use of the following equations (Eqs. (10) and (11)). This evaluation produced the maximum dispersion direction (third eigenvector), which corresponds to the longitudinal axis of the bridge. A rotation along the z-axis was performed with the aim of aligning the x-axis of the point cloud with the longitudinal axis of the bridge (Fig. 17).

$$V_i = \frac{1}{n-1}\sum_{m=1}^{n}\left(X_{im} - \overline{X}_i\right)^2 \tag{10}$$

$$C_{ij} = \frac{1}{n-1}\sum_{m=1}^{n}\left(X_{im} - \overline{X}_i\right)^2\left(X_{jm} - \overline{X}_j\right)^2 \tag{11}$$

where V_i and C_{ij} are the variance and the covariance of each variable i and j; n is the number of points of the data matrix from the point cloud, $\sum_{m=1}^{n}$ is the sum over all n points; X_{im} is the value of each variable i; X_{jm} is the value of each variable j; $\overline{X}_i$ is the mean of the variable i and; $\overline{X}_j$ is the mean of the variable j.

In the second step, the multistep geometrical modelling method proposed by [24] was used. This methodology is based on the following stages: (i) Delaunay triangulation of the aligned point cloud, (ii) hole filling based on radial basis functions [25], (iii) topological noise removal via local re-triangulation [26], (iv) segmentation of the different structural components, and (v) adjustment of the segmented elements into basic primitives based on linear and non-linear (b-splines) extrusions. As a result, a mesh composed of a total of 9,567,843 triangles was transformed into a suitable and accurate CAD model of the bridge for subsequent numerical simulations (Fig. 18).

Finally, the FEM method was applied in the CAD model to perform further numerical simulations using the software TNO Diana® [27]. As a result, a mesh composed of a total of 128,884 elements was obtained (Fig. 19) including (i) 127,089 solid elements for the structural components and (ii) 1,795 interface elements for simulating the interaction of the bridge with the soil. This mesh was built assuming the following criteria: (i) maximum size of the element = 1 m, (ii) minimum size = 0.3 m to better represent the geometry of the as-built CAD model, and (iii) a minimum of 2 elements in the thickness direction of the barrel vaults to identify possible non-linearities in further non-linear assessments.

However, although the numerical model is detailed from the point of view of each structural element in the best possible way, certain simplifications were assumed considering the feasibility of the model development and computational cost reduction in subsequent numerical simulations. Thus, the thicknesses of the spandrel walls and barrel vaults was assumed to be constant over the entire height and width, respectively. Furthermore, the wing wall and the reinforced concrete pier were not included in the final model because they can be considered as perfect fixed structures (Figs. 19 and 20).

4.2. First results from the numerical model of the Arco Bridge

Considering the mean values of the mechanical parameters obtained during the experimental campaign (Tables 1, 2 and 7) and assuming boundary conditions in agreement with the bridgés surrounding medium (all degrees of freedom fixed with infinite normal and shear stiffnesses in all interface elements), an initial assessment was performed (Fig. 19). To evaluate the accuracy of the numerical model, two quality indices were considered: (i) the relative error between the numerical and experimental frequencies and (ii) analysis of the discrepancies between modal displacements via the modal assurance criterion (MAC) [28]. The results obtained from the evaluation of the different quality indices revealed a rigid structure (high relative error between frequencies, especially in mode 1) as well as moderate discrepancies in modes 2 and 3 (transversal modes) with respect to the modal displacements (Table 8 and Fig. 20).

According to the previous results (Table 8 and Fig. 20), it was possible to observe selected discrepancies in the first frequency and lower MAC values in the 2nd and 3rd eigenmodes, suggesting the necessity of using an updating method to enhance the results.

For more in-depth evaluation of the origin of the discrepancies in the 2nd and 3rd eigenmodes, the coordinate modal assurance criterion (COMAC) [28] was used. As a result, it was possible to observe a concentration of discrepancies in the following degrees of freedom (Fig. 21): (i) the first degree of freedom in the Y- axis direction and (ii) the fourth and tenth degrees of freedom in the Z-axis direction. These discrepancies correspond with the mid-span of the larger barrel vault as well as an iteration in the soil-bridge (see Section 3.3).

4.3. Numerical model updating strategy

Considering the results obtained in the previous section (Table 8) (Figs. 20 and 21), an updating procedure was conducted. During this procedure, the following stages were considered: (i) global sensitivity analysis and (ii) minimization of the cost function.

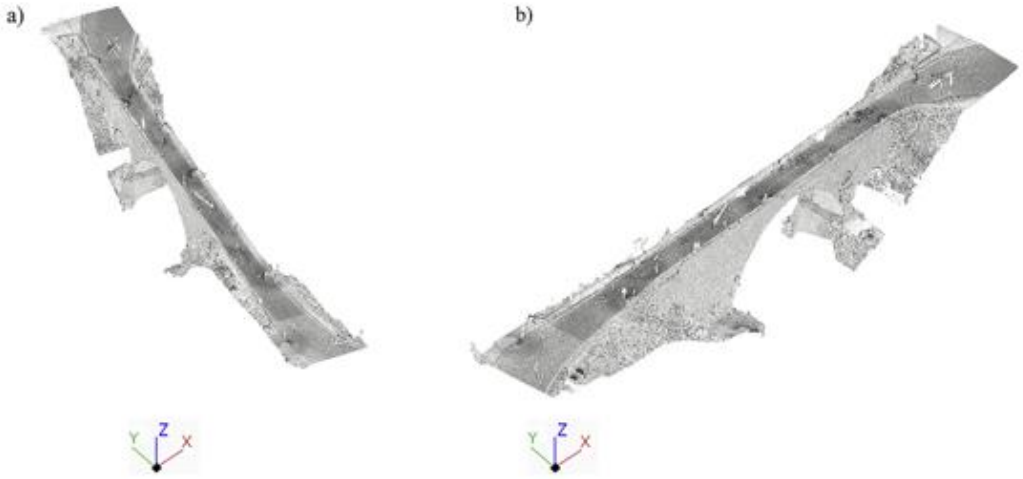

Fig. 17. Results applying the methodology proposed by [5]: a) original point cloud; b) rotated point cloud.

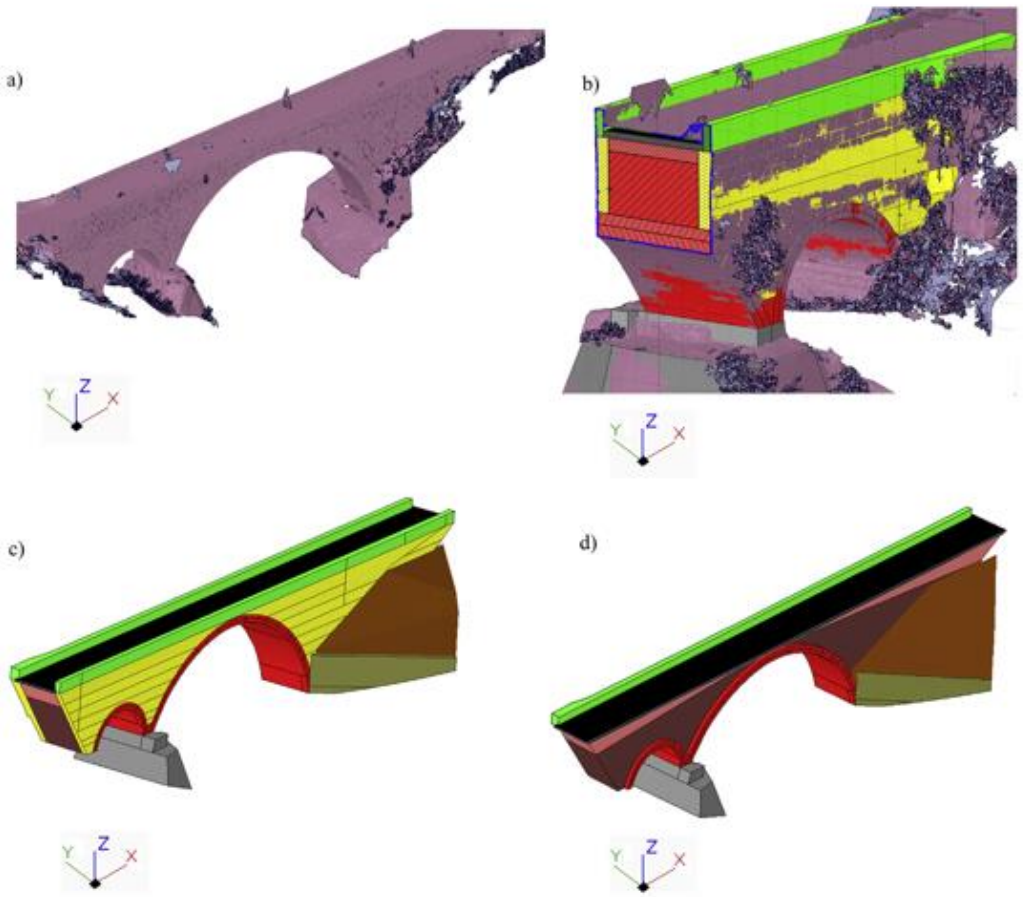

Fig. 18. As-built CAD model obtained: a) isometric view of the mesh obtained from the rotated point cloud; b) detail of the accuracy between the CAD model and the mesh c) isometric view of the as-built CAD model and d) isometric view of the infill material layers.

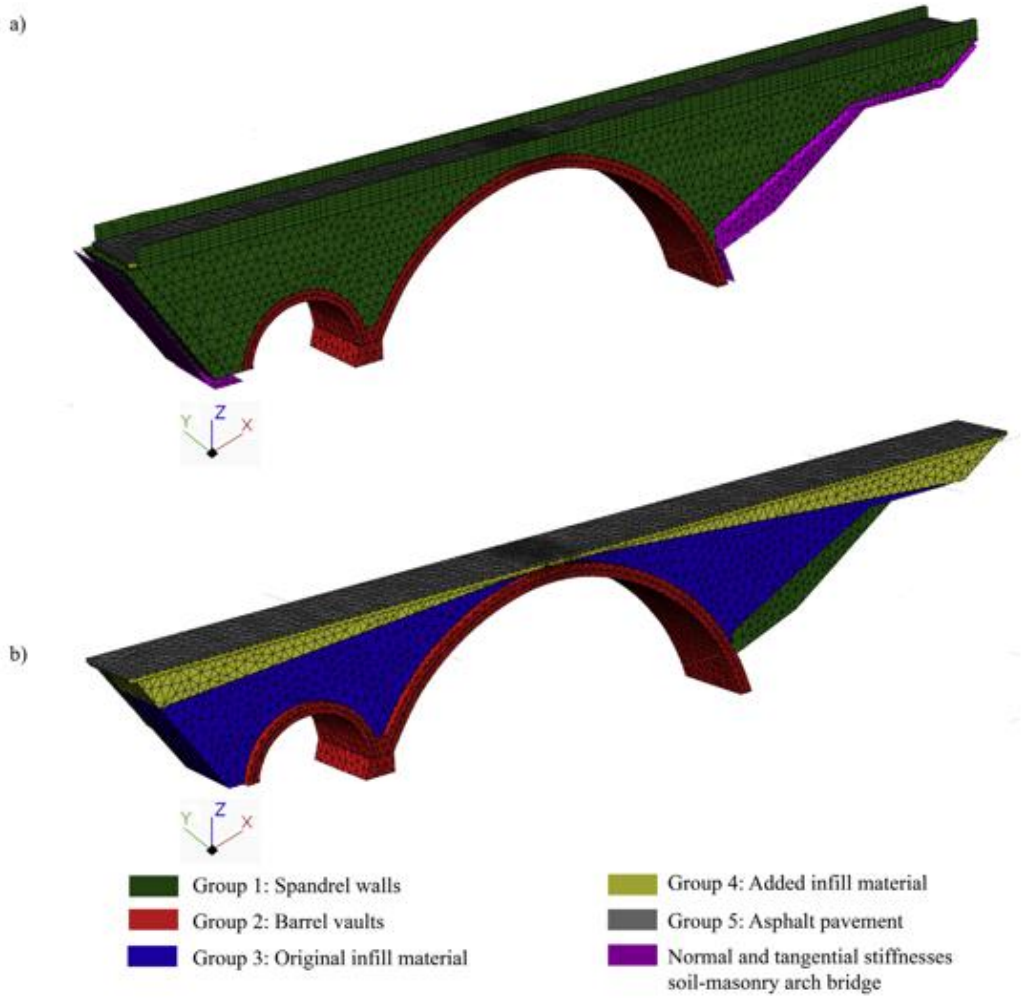

Fig. 19. Mesh model used for the numerical simulations: a) bridgés envelop and b) inner distribution of the bridge.

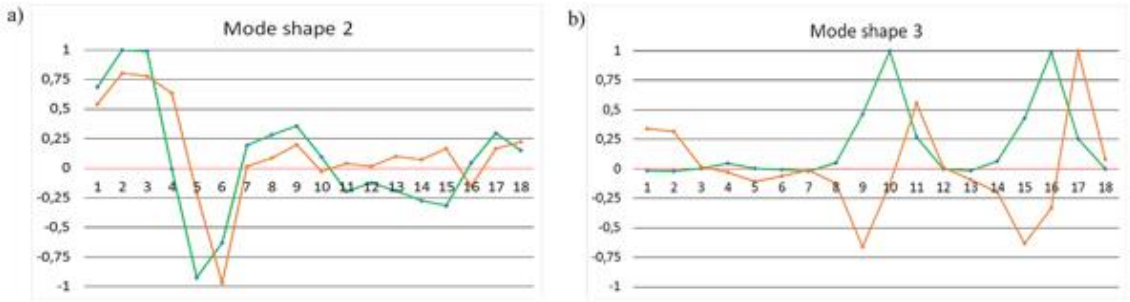

Fig. 20. Comparison between experimental and numerical modal displacements of the mode shape 2 and the mode shape 3. In green the experimental modal displacements and in orange the numerical ones. The vertical axis of the graphs represent the normalized modal displacements and the horizontal axis the degree of freedoms. (For interpretation of the references to colour in this figure legend, the reader is referred to the web version of this article.)

Table 7
Average values of the Youngs modulus and densities calculated from the values obtained during the sonic tests (Groups 1 and 2) and MASW tests (Groups 3 and 4). With respect to the asphalt pavement (Group 5), the average values proposed by Von Quintos [29] were assumed.

Group	Elastic modulus (GPa)	Density (kg/m^3)
Group 1	1.78	2250
Group 2	3.29	2250
Group 3	1.73	1909
Group 4	0.41	1819
Group 5	2.41	2237

4.3.1. A global sensitivity analysis based on the combination of polynomial chaos expansion and Sobol's indices

Global sensitivity analysis is used to determine how the variability of the model response (frequencies and modal displacements) is affected by the value of the input parameters (variables of the model). A common and robust technique is based on the decomposition of the response variance as a sum of contributions that can be associated with each input, i.e., the so-called Sobol's indices [14]. Commonly, these indices are evaluated using Monte Carlo simulations, which require thousands of simulations to obtain reliable results. Therefore, this strategy is non-viable for those cases in which the computational costs of the numerical model are high [15].

As such, a reliable alternative is the use of the so-called surrogate models. These models are compact and scalable analytical models that approximate the input output response of a complex system, i.e., in this case, advanced numerical simulation approximations of the original computational model requiring only a limited number of runs to obtain accurate results (Eq. (12)).

$$x \epsilon D_x \subset R^d \rightarrow y = f(x) \tag{12}$$

where $\times$ are the input parameters; D_x the space of these parameters, y the output of the subrogate and $f(x)$ the subrrogate model.

Of the wide variety of metamodels that are currently available, from Kriging metamodels to radial basis functions [30], the polynomial chaos expansion (PCE) is one of the most used options. This approach evaluates the sensitivity indices and their iterations [30] and assumes that the numerical simulation can be represented as a finite variance model $M(X)$ whose inputs x are a random vector of independent constrained variables $X \in \square^M$. Each of these inputs is described as a joint probability density function (PDF) fx, and therefore, the computational model can be represented by the following equation (Eq. (13)).

$$Y \approx f(X) = \sum_{\alpha \in N^M} y_\alpha \psi_\alpha(X) \tag{13}$$

where Y is the computational model, $\psi_\alpha(X)$ is the multivariate orthonormal polynomial with respect to $fx(x)$, $\alpha \in \mathbb{N}^M$ is a multi-index that locates the components of the multivariate polynomials ψ_α and the $y_\alpha \in \mathbb{R}$ are the respective coefficients (coordinates) and; M is the number of input variables.

From a practical point of view, the sum of Eq. (13) must be truncated to a finite sum of the truncated polynomial chaos expansion (Eq. (14)) [31]:

$$Y \approx \tilde{f}^{PCE}(X) = \sum_{\alpha \in A} y_\alpha \psi_\alpha(X) \tag{14}$$

where $M^{PCE}(X)$ is the polynomial chaos expansion surrogate model; $\alpha = \{\alpha_1 \ldots \alpha_d\}$ are the indexes of the polynomial chaos expansion; $A \in \mathbb{N}^M$ is the set of indexes α corresponding to the truncation scheme; $X = (X_1, X_2, \ldots, X_d)$ is the multivariate vector of the input parameters considered and $\psi_\alpha$is the multivariate polynomial.

Table 8
MAC values and numerical frequencies obtained from the initial model compared with the experimental frequencies obtained from the AVT.

Vibration modes	*fexp* (Hz)	*fnum* (Hz)	Relative error (%)	MAC
1	5.56	5.31	4.45	0.95
2	8.22	8.11	1.37	0.80
3	9.31	9.48	1.81	0.82
4	11.47	11.36	0.95	0.96
5	18.09	18.02	0.40	0.87

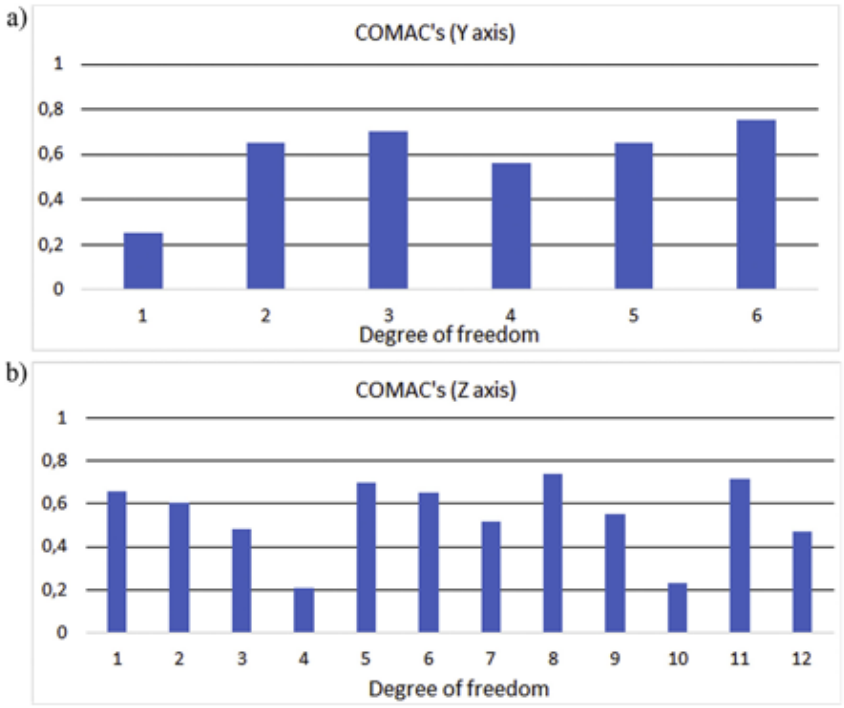

Fig. 21. COMAC values obtained from the first simulation: a) COMAC values in Y axis and b) COMAC values in Z axis.

Moreover, the multivariate polynomials (ψ_α) that include the PCE basis are obtained through the tensorization of suitable univariate polynomials. It is worth mentioning that each univariate polynomial was constructed using the classical families of polynomial proposed by [32]. Legendre polynomials were applied for those inputs with uniform PDFs, and Hermite polynomials were chosen for inputs with Gaussian PDFs. Multivariate polynomials $(\psi_\alpha)(\chi)$ are assembled as the tensor product of their univariate polynomials. For calculation of the coefficients, we used a non-intrusively strategy based on the least-square minimization proposed by [33].

The set of multi-indices A of Eq. (14) is obtained using a suitable truncation scheme, which consists of selection of multivariate polynomials up to a total degree p^t, i.e., $\{\psi_\alpha, \alpha \in \mathbb{N}^{M:} \sum_{i=1}^{M} \alpha_i \leq p^t\}$. Therefore, the corresponding number of terms in the truncated series is defined as shown (Eq. (15)):

$$cardA = \binom{M+p^t}{p^t} = \frac{(M+p^t)!}{M!p^t!} \tag{15}$$

where M are the input variables of the polynomial; and p the degree of the polynomials.

It is important to highlight that the truncated polynomial chaos expansion shown in (Eq. (13)) can be decomposed into summands of increasing order, similar to the definition of the Sobol's indices. For any non-empty set $u \subset \{1, \ldots, M\}$ and any finite truncation set $A \subset \mathbb{N}^M$, it can be stated that $A_u = \{\alpha \in A : k \in u \Leftrightarrow \alpha_k \neq 0, k = 1,\ldots M\}$. This statement means that A_u encompasses all multi-indices within the truncation set A that have non-zero components $\alpha_k \neq 0$ if and only if $k \in u$. Moreover, the sum of the associated terms from the PCE creates a function that depends only on the input variables x_u. Due to the orthonormality of the PCE, the variance of the truncated model can be expressed as shown (Eqs. (16) and (17)):

$$Var[Y_A] = \sum_{\substack{\alpha \in A \\ \alpha \neq 0}} \hat{y}_\alpha^2 \tag{16}$$

$$Var[f_v(X_v)] = \sum_{\substack{\alpha \in A \\ \alpha \neq 0}} \hat{y}_\alpha^2 \tag{17}$$

where Y_A is the truncated model; and $f_v(x_v)$ is the expresion of each summand for the polynomial chaos expansion.

Considering the expressions previously shown, the Sobol's indices can be expressed as follows (Eqs. (18) and (19)):

$$\widehat{S}_i = \frac{\sum_{\alpha \in A_i} \widehat{y}_\alpha^2}{\sum_{\alpha \in A, \alpha \neq 0} \widehat{y}_\alpha^2} \quad \text{where } A_i = \{\alpha \in A : \alpha_i > 0, \alpha_{j \neq i} = 0\} \tag{18}$$

$$\widehat{S}_i^T = \frac{\sum_{\alpha \in A^T} \widehat{y}_\alpha^2}{\sum_{\alpha \in A, \alpha \neq 0} \widehat{y}_\alpha^2} \quad \text{where } A_i^T = \{\alpha \in A : \alpha_i > 0\} \tag{19}$$

where $\hat{S}_i$ and $\hat{S}_i^T$ are the first-order and total Sobol's indices of the output variable i; $\hat{y}$ and α are the coefficients and indices of the polynomial chaos expansion, respectively; and A is the subset of input variables. The first-order Sobol's indices $\hat{S}$ i represent the effect of each input variable alone in the model variance. Additionally, the total Sobol's indices represent the full effect of each input variable (alone and in combination with other input variables) in the output model variance.

According to the previously defined approach, a total of 100 metamodels were built to evaluate the first five frequencies and the associated modal displacements (90 for each mode). Furthermore, validation of these metamodels was conducted using the leave-one-out error (LOO error) (Eq. (20)) [34,35].

$$LOO\ error = \frac{1}{N} \sum_{i=1}^{N} \left(\frac{Y\left(X^{(i)}\right) - \tilde{f}^{PCE}\left(X^{(i)}\right)}{1 - h_i} \right)^2 \tag{20}$$

where $Y\left(X^{(i)}\right)$ is the computational model; $\tilde{f}^{PCE}\left(X^{(i)}\right)$ is the subrogate model obtained from a specific DoE with N samples and; h_i is the i–th diagonal term of matrix $A(A^TA)^{-1}A^T$; and A the experimental matrix.

The relative LOO error (err_{LOO}) is obtained from the normalization of the *LOO error* (Eq. (20)) with the empirical variance of the set of model evaluations at the experimental design $Y = \{Y\left(X^{(i)}\right), \cdots, Y\left(X^{(N)}\right)\}$. Considering that the estimate of this error may be too optimistic, a corrected estimate proposed by [36] was used (Eq. (21)).

$$errLOO^* = errLOO\left(1 - \frac{cardA}{N}\right)^{-1}\left(1 + tr\left(\psi^T\psi\right)^{-1}\right) \tag{21}$$

where *card A* is the number of terms in the truncated series; and $\psi = \{\psi_{ij} = \psi_j(x^{(i)}),\ i = 1, \cdots, N; j = 1, \cdots, cardA\}$.

This metric of error offers a good compromise between fair error estimation and affordable computational cost.

4.3.2. The minimization strategy

Once the most sensitive variables were obtained, the subsequent step minimized the discrepancies between the numerical and the experimental data. To this end, the following cost function was considered (Eq. (22)).

$$\pi = \frac{1}{2}\left[W_f \sum_{i=1}^{n} \left(\frac{f_{i,num}^2 - f_{i,exp}^2}{f_{i,exp}^2} \right)^2 + W \sum_{j=1}^{m} (1 - MAC)^2 \right] \tag{22}$$

where π is the cost function to be minimized, which is composed of the residuals of the relative error between the numerical $f_{i,num}$ and experimental frequencies $f_{i,exp}$ as well as the MAC values. The terms n and m of this cost function represent the number of frequencies and mode shapes assumed in the calibration of the numerical model, respectively, whereas W_f is the frequency weight, and W is the MAC weight. To balance the contributions of the frequencies and MAC of the residuals of the objective function, the values for the W_f and the W were assumed to be three and one, respectively.

Considering the possible non-linear relationship between the residuals of the cost function and the input variables, the minimization problem was formulated as a non-linear least-squares problem using the iterative Gauss-Newton method to minimize the cost function (LS). This method was complemented by the trust region reflective algorithm, as previously proposed [13]. Within this iterative minimization problem, the gradient and the Hessian of the objective function were calculated as follows (Eqs. (23) and (24)):

$$\nabla\pi(\theta) = J(\theta)^T r(\theta) \tag{23}$$

$$\nabla^2(\theta) = J(\theta)^T J(\theta) + \sum_{i=1}^{k} r_i(\theta)\nabla^2 r_i(\theta) \cong J(\theta)^T J(\theta) \tag{24}$$

where r is the k -dimensional vector of the frequency and mode shape residuals, θ represents the vector of input variables, and J indicates the Jacobian or sensitivity matrix containing the first partial derivatives of the residuals with respect to the input variables. These derivatives were calculated via the finite difference strategy.

Considering that the previously shown optimization strategy is a local minimization method, and with the aim of finding the global minimum of the cost function, a multi-start approach was chosen. This approach runs several optimization prob-

Table 9
Upper and lower bounds considered during the updating stage. The upper and lower bounds of the supports stiffnesses, the Young Modulus (*E5*) and the density (*d5*) of the asphalt pavement were extracted from Chen & Bathurst [39] and Von Quintus [29], respectively.

Parameter	Upper bounds	Lower bounds
E1 (GPa)	2.56	1.00
E2 (Gpa)	4.00	2.57
E3 (Gpa)	3.18	0.56
E4 (Gpa)	0.78	0.33
d1 (kg/m^3)	2500	2000
d2 (kg/m^3)	2500	2000
Kn1 (N/m^3)	1.00×10^8	1.00×10^6
$Kt1_x$ (N/m^3)	1.00×10^8	1.00×10^6
$Kt1_y$ (N/m^3)	1.00×10^8	1.00×10^6
Kn2 (N/m^3)	1.00×10^8	1.00×10^6
$Kt2_x$ (N/m^3)	1.00×10^8	1.00×10^6
$Kt2_y$ (N/m^3)	1.00×10^8	1.00×10^6

lems, beginning each from a different initial point. These initial points were created with the Latin hypercube sampling method (LHS) [37].

4.4. Calibrated model

With the workflow proposed in the previous section, an updating process for the previously defined numerical model was conducted (Fig. 19). To this end, an initial set of variables was considered: (i) four Young's modulus (*E1–E4*) values corresponding to the groups of masonry and infill materials (Table 7); (ii) two densities (*d1* and *d2*) corresponding to the masonry of the spandrel walls and barrel vaults and; (iii) two normal stiffnesses (*Kn1* and *Kn2*) and four shear stiffnesses in the X-direction and Y-direction ($Kt1_x$, $Kt1_y$ and $Kt2_x$, $Kt2_y$) at the extremes of the bridge to simulate the possible interaction between the bridge and the soil. The inputs *d3* (density of the added infill layer), *d4* (density of the original infill layer), *E5*, *d5* (the Young Modulus and density of the pavement) were not considered during the sensitivity analysis with the aim of reducing the complexity of the surrogate model. Additionally, *d3* and *d4* were not considered due to their low variance compared with the remainder of variables (Table 1). However, *d5* and *E5* were not included because it is expected that their contribution is low compared with the variables previously cited.

With this set of variables and under the premises defined in Section 4.3.1, different PCE-metamodels were built to evaluate the Sobol's indices of each output variable (5 frequencies and 90 modal displacements). In these evaluations, different sample sizes were considered to generate the optimum metamodel of each output (best relationship between the number of evaluations and the accuracy of the model). The samples of the DoE were extracted in a sequential manner using the sequential Latin hypercube sampling (LHS) methodology, as proposed by [38]. This stage used the constriction of the upper and lower bounds of the variables obtained during the experimental campaign (Table 9).

According to Table 10, it was possible to conclude that the optimum design of experiment (DoE) value of the metamodel is 500, showing an average LOO error of 2.19×10^{-3}. This DoE corresponds to 50 times the number of input variables used as inputs to represent the response of the numerical model. Therefore, PCE metamodels built with 500 samples were considered for calculation of the Sobol's indices (Fig. 22).

Table 10
LOO error in frequencies output variables and average LOO error in modal displacements output variables for different sizes of the DoE. Dm_i is the average value of the modal displacements for the mode *i*.

	Number of samples obtained with the LHS					
Output variable	100	200	300	400	500	600
f1	5.27×10^2	1.80×10^{-2}	7.48×10^{-3}	1.06×10^{-5}	3.17×10^{-6}	1.14×10^{-6}
f2	3.06×10^2	2.16×10^{-2}	1.38×10^{-2}	1.73×10^{-5}	6.76×10^{-6}	8.21×10^{-6}
f3	1.90×10^{-1}	1.02×10^{0}	1.01×10^{0}	1.01×10^{-1}	8.90×10^{-5}	8.12×10^{-5}
f4	3.93×10^3	2.37×10^{-2}	2.25×10^{-2}	3.32×10^{-4}	1.37×10^{-5}	1.43×10^{-5}
f5	1.69×10^{-2}	4.26×10^{-1}	4.12×10^{-1}	3.71×10^{-3}	2.57×10^{-5}	1.36×10^{-5}
dm1	2.18×10^3	1.65×10^{-1}	1.09×10^{-1}	9.08×10^{-4}	5.78×10^{-5}	4.17×10^{-5}
dm2	3.83×10^2	4.94×10^{-1}	4.99×10^{-1}	4.53×10^{-4}	3.30×10^{-4}	3.71×10^{-4}
dm3	3.08×10^3	4.71×10^{-1}	4.59×10^{-1}	3.85×10^{-1}	5.04×10^{-3}	4.76×10^{-3}
dm4	6.10×10^5	8.63×10^{-1}	8.09×10^{-1}	7.76×10^{-3}	7.84×10^{-3}	7.57×10^{-3}
dm5	3.77×10^4	9.96×10^{-1}	8.75×10^{-1}	9.34×10^{-3}	8.46×10^{-3}	8.60×10^{-3}

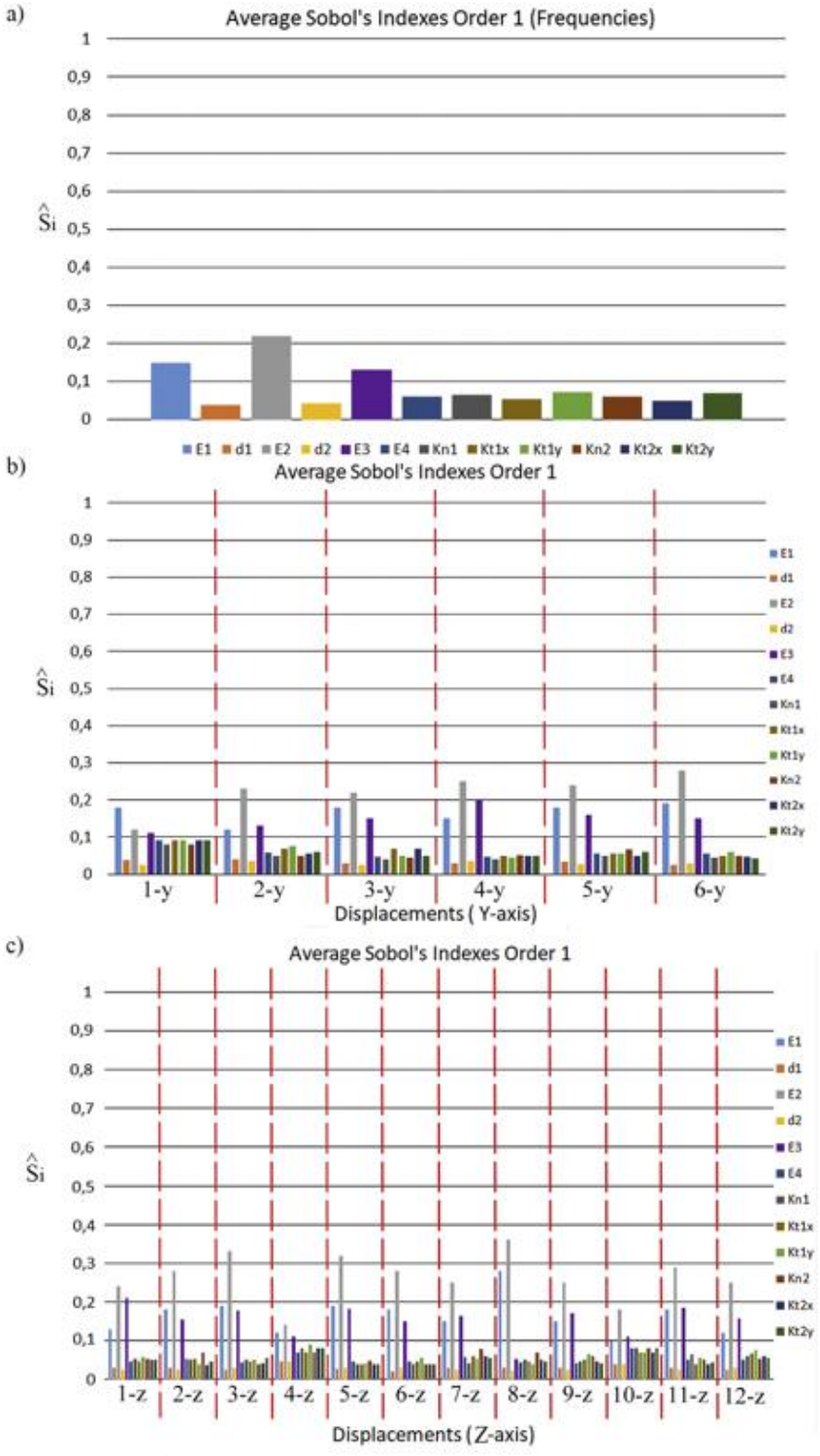

Fig. 22. Average first order Sobol's indexes ($\hat{S}_i$) obtained during the global sensitivity analysis of the numerical model: a) Average first order Sobol's indexes of the first five eigenfrequencies; b) Average first order Sobol's indexes of the Y-axis modal displacements and c) Average first order Sobol's indexes of the Z-axis modal displacements.

Table 11
Values of each one of the 20 samples coming from the LHS method obtained for the sensitive parameters. These values were used as starting points during the calibration of the numerical model of the bridge.

Sample	*E1* (GPa)	*E2* (GPa)	*E3* (GPa)	*E4* (GPa)	*Kn1* (N/m^3)	$Kt1_x$ (N/m^3)	$Kt1_y$ (N/m^3)	*Kn2* (N/m^3)	$Kt2_x$ (N/m^3)	$Kt2_y$ (N/m^3)
1	2.03	3.32	1.23	0.42	5.27×10^7	6.54×10^7	6.54×10^7	3.28×10^7	2.26×10^7	2.26×10^7
2	2.54	2.24	1.81	0.32	4.31×10^7	2.31×10^7	2.31×10^7	5.21×10^7	1.45×10^7	1.45×10^7
3	1.47	3.93	1.98	0.39	2.13×10^7	1.37×10^7	1.37×10^7	4.31×10^7	3.51×10^7	3.51×10^7
4	2.45	3.17	1.65	0.47	3.71×10^7	5.76×10^7	5.76×10^7	2.56×10^7	2.29×10^7	2.29×10^7
5	1.81	2.61	1.49	0.34	1.82×10^7	2.67×10^7	2.67×10^7	1.38×10^7	1.15×10^7	1.15×10^7
6	1.07	3.41	1.70	0.53	6.31×10^7	5.83×10^7	5.83×10^7	3.17×10^7	2.62×10^7	2.62×10^7
7	1.30	3.16	1.33	0.36	7.11×10^7	4.41×10^7	4.41×10^7	5.21×10^7	3.45×10^7	3.45×10^7
8	1.67	3.57	1.03	0.56	4.38×10^7	3.16×10^7	3.16×10^7	2.68×10^7	1.93×10^7	1.93×10^7
9	2.39	3.26	1.85	0.37	2.94×10^7	2.77×10^7	2.77×10^7	1.81×10^7	1.35×10^7	1.35×10^7
10	2.17	3.78	1.63	0.53	3.55×10^7	2.91×10^7	2.91×10^7	2.64×10^7	2.12×10^7	2.12×10^7
11	2.09	3.69	1.20	0.34	1.71×10^7	1.28×10^7	1.28×10^7	2.96×10^7	1.73×10^7	1.73×10^7
12	1.65	3.89	1.07	0.38	2.94×10^7	2.33×10^7	2.33×10^7	3.52×10^7	2.51×10^7	2.51×10^7
13	1.29	2.82	1.15	0.31	4.21×10^7	3.27×10^7	3.27×10^7	5.13×10^7	3.47×10^7	3.47×10^7
14	1.80	3.11	1.61	0.45	5.16×10^7	4.71×10^7	4.71×10^7	4.67×10^7	2.95×10^7	2.95×10^7
15	1.41	2.72	1.23	0.51	2.73×10^7	1.56×10^7	1.56×10^7	3.21×10^7	2.67×10^7	2.67×10^7
16	1.97	3.86	1.74	0.44	3.51×10^7	2.73×10^7	2.73×10^7	4.15×10^7	2.38×10^7	2.38×10^7
17	1.58	3.25	1.29	0.41	2.19×10^7	1.91×10^7	1.91×10^7	3.67×10^7	2.14×10^7	2.14×10^7
18	1.38	3.09	1.78	0.47	1.87×10^7	1.76×10^7	1.76×10^7	2.44×10^7	1.65×10^7	1.65×10^7
19	1.51	3.13	1.81	0.49	3.61×10^7	2.73×10^7	2.73×10^7	4.10×10^7	2.42×10^7	2.42×10^7
20	1.31	3.77	1.54	0.56	2.54×10^7	2.21×10^7	2.21×10^7	3.59×10^7	2.67×10^7	2.67×10^7

Table 12
Discrepancies obtained from the second calibration in terms of relative error in frequencies (*f*) and MAC values. In brackets, values obtained from the initial model.

Vibration modes	*fexp* (Hz)	*fnum* (Hz)	Relative error (%)	MAC
1	5.56	5.45	2.03	0.96
		(5.31)	(4.48)	(0.95)
2	8.22	8.27	0.72	0.92
		(8.11)	(1.37)	(0.80)
3	9.31	9.23	0.87	0.90
		(9.48)	(1.81)	(0.82)
4	11.47	11.53	0.56	0.97
		(11.36)	(0.95)	(0.96)
5	18.09	17.76	1.86	0.91
		(18.02)	(0.41)	(0.87)

From the sensitivity analysis, it was possible to conclude that the variance of the output model is strongly influenced by the variance of each input alone because the first-order Sobol's indices are similar to the total Sobol's indices. The frequencies are strongly influenced by the inputs *E1*, *E2* and *E3*, showing average first-order Sobol's indices of 0.15, 0.21 and 0.13, respectively. This result means that 15 %, 21 % and 13 % of the output variance is caused by the variance of these inputs. For the modal displacements, it was possible to observe that the inputs *E1*, *E2* and *E3* are the most sensitive variables, with average first-order Sobol's indices of 0.18, 0.26 and 0.17, respectively. For the remaining inputs, it was possible to observe that the different variables that define the interaction bridge-soil have a similar impact on the output variance. The densities (*d1* and *d2)* are the inputs with less impact in the output variance, especially in the frequencies of the model.

Higher average first-order Sobol's indices were obtained in the frequencies (Fig. 22a) for the Young's modulus *E1*, *E2*, and *E3* corresponding to the Group 1 (spandrel walls), Group 2 (barrel vaults) and Group 3 (original infill material), respectively, as the most initially sensitive parameters. With the aim of identifying more parameters with high sensitivity, the degrees of freedom (DOF) with lower COMAC values from the initial model were associated with the corresponding DOF of the average first-order Sobol's indices of the displacements (the first DOF in the Y-axis direction and the fourth and tenth DOF in the Z-axis direction) (Figs. 21 and 22b, c). This approach identified the Young's modulus *E4* corresponding to the Group 4 (added infill material) and all stiffnesses that represent the interaction between the bridge and the soil ($Kn1$, $Kt1_x$, $Kt1_y$, $Kn2$, $Kt2_x$ *and* $Kt2_y$) as the most sensitive parameters together with *E1*, *E2* and *E3*. Therefore, a total of 10 parameters were considered for the subsequent updating process. During this stage, we used the average values of the inputs *d1*, *d2*, *d3*, *d4*, *d5* and *E5* to calibrate the model (Tables 1 and 7).

Finally, minimization of the cost function was performed via the optimization strategy defined in Section 4.3.2 (LHS + LS). In this case, a total of 20 samples from the LHS method were considered as starting points for the minimization problem (Table 11). As a result of these 20 minimizations, it was possible to find a minimum for which the numerical model showed an average relative error in frequencies of 1.21% and an average MAC value of 0.93 (Table 12). The updated values of the

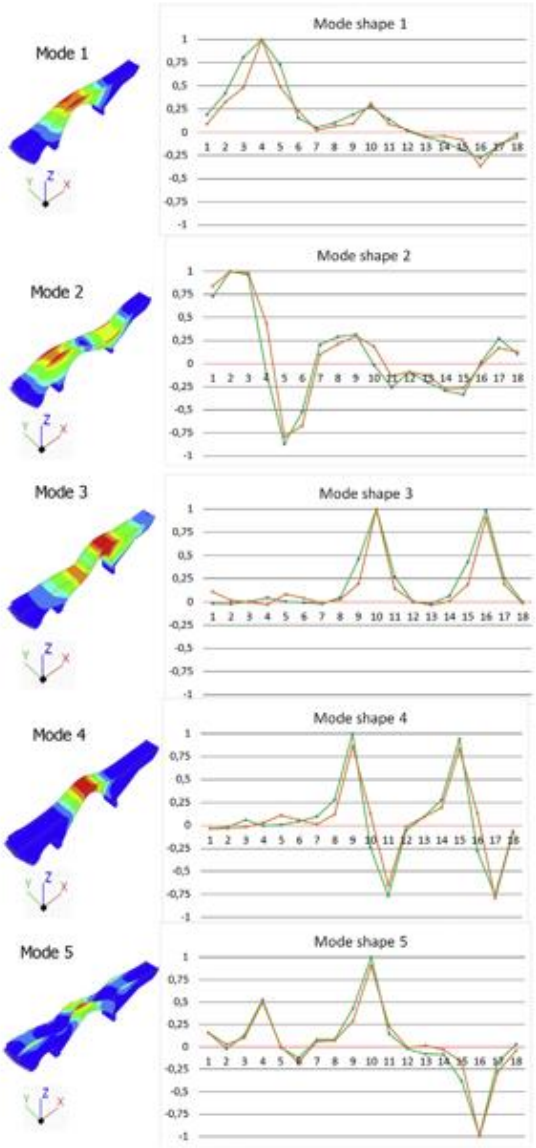

Fig. 23. Graphical comparison between experimental (green) and numerical (orange) modal shapes obtained from the updated numerical model. The horizontal axis of the graphs represent the degree of freedoms and the vertical axis the normalized modal displacements. (For interpretation of the references to colour in this figure legend, the reader is referred to the web version of this article.)

masonry structural elements and the infill materials of the numerical model (Table 12) are approximated with respect to the average values obtained from the experimental campaign (Tables 1 and 2), corroborating the robustness of the calibrated numerical model and the experimental tests conducted on the bridge (MASW and sonic tests).

Finally, Fig. 23 reveals a comparison between the experimental and numerical mode shapes from a graphic point of view (Fig. 16). Finally, (Table 13) (Fig. 16), the results obtained from the updated numerical model present a better correlation for the experimental results obtained from the AVT, especially with respect to the discrepancies observed in the 2nd and 3rd vibrational modes, which improved their MAC values from an initial value of 0.80 and 0.82 for the 2nd and 3rd modes to 0.92 and 0.90, respectively. This result re-affirmed the importance of the influence of the boundary conditions on the dynamic behaviour of the bridge.

Table 13
Comparison between the initial numerical model and the updated numerical model.

Parameter	Upper bounds	Lower bounds	Initial numerical model	Updated numerical model
E1 (GPa)	2.56	1.00	1.79	1.91
E2 (GPa)	4.00	2.57	3.28	3.62
E3 (GPa)	3.18	0.56	1.73	0.97
E4 (GPa)	0.78	0.33	0.41	0.51
$Kn1$ (N/m^3)	1.00×10^8	1.00×10^6	–	1.88×10^7
$Kt1_x$ (N/m^3)	1.00×10^8	1.00×10^6	–	1.83×10^7
$Kt1_y$ (N/m^3)	1.00×10^8	1.00×10^6	–	1.83×10^7
$Kn2$ (N/m^3)	1.00×10^8	1.00×10^6	–	3.34×10^7
$Kt2_x$ (N/m^3)	1.00×10^8	1.00×10^6	–	1.01×10^7
$Kt2_y$ (N/m^3)	1.00×10^8	1.00×10^6	–	1.01×10^7

5. Conclusions

This paper proposes a robust multidisciplinary approach used to obtain accurate numerical simulations of masonry arch bridges via the finite element method. This methodology, which is fully based on non-destructive methods, enhances the current multidisciplinary methods for structural assessment of masonry bridges at different levels.

At the material and geometrical levels, the proposed methodology considers the use of several wave-based approaches, such as multichannel analysis of surface waves or sonic testing, with the aim of accurately characterizing the different materials presented in the bridge compared with the traditional multidisciplinary methodology. It is worth mentioning that the values obtained for the "original infill layer" can be justified by the presence of selected intrusions of natural soil within the space delimited by the spandrel walls. The combination of the terrestrial laser scanner and ground-penetrating radar with reverse engineering procedures allowed creation of as-built CAD models of masonry bridges. This methodology is able to reproduce possible non-parametric shapes presented in this type of structure in contrast with other methodologies in which the CAD model is created via extraction of a section from the point cloud. Additionally, the proposed methodology was able to characterize the mechanical and physical properties of the infill without requiring the use of values from the literature or the application of invasive methods based on extraction of samples, as in other multidisciplinary approaches.

For the numerical field, the finite element model derived from the proposed methodology shows good correlation with respect to the ground truth (ambient vibration tests). This model shows an error in frequencies of approximately 1.80% and an average MAC value of 0.88, demonstrating the robustness of the multidisciplinary approach. This correlation was enhanced due to the use of an updating method based on the combination of a polynomial chaos expansion metamodel and Sobol's indices for the sensitivity analysis as well as a non-linear least squares optimization approach. The great efficiency and accuracy of the polynomial chaos expansion metamodel for the sensitivity analysis lies in the requirement of a low number of iterations compared with the classical Monte Carlo approach. In our case, considering that 10 input variables were used to build the surrogate model, we needed a total of 500 points for the DoE (approximately 50 times the number of variables). Additionally, the ability to analyse the Sobol's indices from the polynomial chaos expansion allow us to evaluate the influence of each input in the output variance in a robust manner, instead of using basic sensitivity analysis or correlation methods (e.g., the Spearman matrix).

This updating approach created a numerical model with a relative error in frequencies of 1.21% and an average MAC value of 0.93. During this stage, and considering the nature of the optimization algorithm used, which is prone to becoming trapped in local optima, a total of 20 optimization runs were conducted with the aim of exploring the search space and obtaining a possible global minimum. The starting point of each run was obtained via the LHS method. Each run required 4836 seconds to reach the minimum and thus, a total of 109,320 seconds was spent during the updating stage: i) 12,600 seconds for the sensitivity analysis (PCE + Sobol) and ii) 96,720 seconds for the optimization (non-linear squares + Gauss-Newton) on a system with a Intel® XEON E3-1240 v3 processor running at 3.4 GHz with 8 GB RAM DDRII.

Finally, we offer several options for future work in several fields. Different numerical analyses will be conducted with the aim of evaluating the current structural performance against static (traffic loads) and dynamic (such as earthquakes) situations as well as the use of adaptive sampling strategies, such as those proposed by [40] based on the LOLA-VORONOI algorithm. Additionally, further research will be focused on an in-depth evaluation of the MASW method with the aim of characterizing the non-linear properties of the infill, i.e., the (i) cohesion and (ii) friction angle, as well as the use of additional methods such as electric resistivity tomography to obtain an in-depth evaluation of the bridge infill topology. Additionally, considering the uncertainty associated with the data obtained by the 250 MHz GPR antenna, several impact-echo tests will be performed on the barrel vaults and asphalt with the aim of corroborating the thicknesses supplied by GPR and historical drawings. Finally, several radiometric classifications based on the data acquired from the TLS system will be performed to complete damage evaluation of the construction using pixel-based classification methods.

Acknowledgments

This work was financed by ERDF funds through the V Sudoe Interreg program within the framework of the HeritageCARE project, Ref. SOE1/P5/P0258. This research has been also partially supported by Patrimonio 5.0 funded by Junta of Catilla y León, Ref. SA075P17. Second author would like to thank the University of Salamanca for the program for human resources "Programa II: Contratos Postdoctorales".

References

[1] B. Conde, L.F. Ramos, D.V. Oliveira, B. Riveiro, M. Solla, Structural assessment of masonry arch bridges by combination of non-destructive testing techniques and three-dimensional numerical modelling: application to Vilanova bridge, Eng. Struct. 148 (2017) 621–638, https://doi.org/10.1016/j.engstruct.2017.07.011.
[2] B. Riveiro, J. Caamaño, P. Arias, E. Sanz, Photogrammetric 3D modelling and mechanical analysis of masonry arches: an approach based on a discontinuous model of voussoirs, Autom. Constr. 20 (2011) 380–388, https://doi.org/10.1016/j.autcon.2010.11.008.
[3] D. Ribeiro, R. Calçada, R. Delgado, M. Brehm, V. Zabel, Finite element model updating of a bowstring-arch railway bridge based on experimental modal parameters, Eng. Struct. 40 (2012) 413–435, https://doi.org/10.1016/j.engstruct.2012.03.013.
[4] M. Stavroulaki, B. Riveiro, G. Drosopoulos, M. Solla, P. Koutsianitis, G.E. Stavroulakis, Modelling and strength evaluation of masonry bridges using terrestrial photogrammetry and finite elements, Adv. Eng. Softw. 101 (2016) 136–148, https://doi.org/10.1016/j.advengsoft.2015.12.007.
[5] , Constr. Build. Mater. 158 (2018) 961–984, https://doi.org/10.1016/j.conbuildmat.2017.10.084.
[6] L.F. Miranda, J. Rio, J.M. Guedes, A. Costa, Sonic Impact Method–A new technique for characterization of stone masonry walls, Constr. Build. Mater. 36 (2012) 27–35, https://doi.org/10.1016/j.conbuildmat.2012.04.018.
[7] S. Russo, Integrated assessment of monumental structures through ambient vibrations and ND tests: the case of Rialto Bridge, J. Cult. Heritage 19 (2016) 402–414, https://doi.org/10.1016/j.culher.2016.01.008.
[8] A.S. Gago, J. Alfaiate, A. Lamas, The effect of the infill in arched structures: Analytical and numerical modelling, Eng. Struct. 33 (2011) 1450–1458, https://doi.org/10.1016/j.engstruct.2010.12.037.
[9] B. Conde, L. Díaz-Vilariño, S. Lagüela, P. Arias, Structural analysis of Monforte de Lemos masonry arch bridge considering the influence of the geometry of the arches and fill material on the collapse load estimation, Constr. Build. Mater. 120 (2016) 630–642, https://doi.org/10.1016/j.conbuildmat.2016.05.107.
[10] B. Conde, G. Drosopoulos, G. Stavroulakis, B. Riveiro, M. Stavroulaki, Inverse analysis of masonry arch bridges for damaged condition investigation: application on Kakodiki bridge, Eng. Struct. 127 (2016) 388–401, https://doi.org/10.1016/j.engstruct.2016.08.060.
[11] V. Compan, P. Pachón, M. Cámara, Ambient vibration testing and dynamic identification of a historical building. Basilica of the Fourteen Holy Helpers (Germany), Procedia Engineering 199 (2017) 3392–3397, https://doi.org/10.1016/j.proeng.2017.09.572.
[12] L.J. Sánchez-Aparicio, B. Riveiro, D. Gonzalez-Aguilera, L.F. Ramos, The combination of geomatic approaches and operational modal analysis to improve calibration of finite element models: a case of study in Saint Torcato Church (Guimarães, Portugal), Constr. Build. Mater. 70 (2014) 118–129, https://doi.org/10.1016/j.conbuildmat.2014.07.106.
[13] L.J. Sánchez-Aparicio, L.F. Ramos, J. Sena-Cruz, J.O. Barros, B. Riveiro, Experimental and numerical approaches for structural assessment in new footbridge designs (SFRSCC–GFPR hybrid structure), Compos. Struct. 134 (2015) 95–105, https://doi.org/10.1016/j.compstruct.2015.07.041.
[14] I.M. Sobol, Sensitivity estimates for nonlinear mathematical models, Math. Modell. Comput. Exp. 1 (1993) 407–414.
[15] B. Sudret, Global sensitivity analysis using polynomial chaos expansions, Reliab. Eng. Syst. Saf. 93 (2008) 964–979, https://doi.org/10.1016/j.ress.2007.04.002.
[16] E.R. Almeida, Puentes históricos de la provincia de Ávila, Institución Gran Duque de Alba, 2015.
[17] C.B. Park, R.D. Miller, J. Xia, Multichannel analysis of surface waves, Geophysics 64 (1999) 800–808, https://doi.org/10.1190/1.1444590.
[18] C.S. Blázquez, A.F. Martín, P.C. García, D. González-Aguilera, Thermal conductivity characterization of three geological formations by the implementation of geophysical methods, Geothermics 72 (2018) 101–111, https://doi.org/10.1016/j.geothermics.2017.11.003.
[19] L. Miranda, L. Cantini, J. Guedes, A. Costa, Assessment of mechanical properties of full-scale masonry panels through sonic methods. Comparison with mechanical destructive tests, Struct. Control Health Monit. 23 (2016) 503–516, https://doi.org/10.1002/stc.1783.
[20] H. Yoon, H. Song, K. Park, A phase-shift laser scanner based on a time-counting method for high linearity performance, Rev. Sci. Instrum. 82 (2011), https://doi.org/10.1063/1.3600456 075108.
[21] M. Solla, J. Caamaño, B. Riveiro, P. Arias, A novel methodology for the structural assessment of stone arches based on geometric data by integration of photogrammetry and ground-penetrating radar, Eng. Struct. 35 (2012) 296–306, https://doi.org/10.1016/j.engstruct.2011.11.004.
[22] N.J. Carino, The impact-echo method: an overview, Structures, A Struct. Eng. Odyssey 2001 (2001) 1–18, https://doi.org/10.1061/40558(2001) 15.
[23] H. Herlufsen, P. Andersen, S. Gade, N. Møller, Identification techniques for operational modal analysis–an overview and practical experiences, Proceedings of the 1st International Operational Modal Analysis Conference, Copenhagen, 2005.
[24] M. Herrero-Huerta, D. González-Aguilera, P. Rodriguez-Gonzalvez, D. Hernández-López, Vineyard yield estimation by automatic 3D bunch modelling in field conditions, Comput. Electron. Agric. 110 (2015) 17–26, https://doi.org/10.1016/j.compag.2014.10.003.
[25] D. Branch, L.C. Dang, N. Hall, W. Ketchum, M. Melakayil, J. Parrent, M. Troxel, D. Casebeer, D.J. Jeffery, E. Baron, Comparative direct analysis of type Ia supernova spectra. II. Maximum light, Publ. Astron. Soc. Pac. 118 (2006) 560.
[26] I. Guskov, Z.J. Wood, Topological noise removal, 2001 Graphics Interface Proceedings: Ottawa, Canada 2001 (2001) 19.
[27] T. Diana, DIANA finite element analysis, The Netherlands, (2005).
[28] R.J. Allemang, The modal assurance criterion–twenty years of use and abuse, Sound Vib. 37 (2003) 14–23.
[29] H.L. Von Quintus, Asphalt-aggregate Mixture Analysis System, AAMAS, Transportation Research Board, 1991.
[30] M. Asher, B. Croke, A. Jakeman, L. Peeters, A review of surrogate models and their application to groundwater modeling, Water Resour. Res. 51 (2015) 5957–5973, https://doi.org/10.1002/2015WR016967.
[31] R. Ghanem, P. Spanos, Stochastic Finite Elements: A Spectral Approach, Revisited ed., Dover Publications, INC, New York, 2003.
[32] D. Xiu, G.E. Karniadakis, The Wiener-Askey polynomial chaos for stochastic differential equations, SIAM J. Sci. Comput. 24 (2002) 619–644, https://doi.org/10.1016/j.jcp.2010.12.021.
[33] G. Blatman, B. Sudret, Adaptive sparse polynomial chaos expansion based on least angle regression, J. Comput. Phys. 230 (2011) 2345–2367, https://doi.org/10.1137/S1064827501387826.
[34] M. Stone, Cross-validatory choice and assessment of statistical predictions, J. Roy. Stat. Soc.: Ser. B (Methodol.) (1974) 111–147.
[35] S. Geisser, The predictive sample reuse method with applications, J. Am. Stat. Assoc. 70 (1975) 320–328.
[36] G. Deman, K. Konakli, B. Sudret, J. Kerrou, P. Perrochet, H. Benabderrahmane, Using sparse polynomial chaos expansions for the global sensitivity analysis of groundwater lifetime expectancy in a multi-layered hydrogeological model, Reliab. Eng. Syst. Saf. 147 (2016) 156–169.
[37] M.D. McKay, R.J. Beckman, W.J. Conover, Comparison of three methods for selecting values of input variables in the analysis of output from a computer code, Technometrics 21 (1979) 239–245, https://doi.org/10.1080/00401706.1979.10489755.
[38] Z. Liu, M. Yang, W. Li, A Sequential Latin Hypercube Sampling Method for Metamodeling, Theory, Methodology, Tools and Applications for Modeling and Simulation of Complex Systems, Springer (2016) 176–185, https://doi.org/10.1007/978-981-10-2663-8_19.

[39] J. Chen, R. Bathurst, Investigation of interface toe sliding of reinforced soil block face walls using FLAC, Proceedings of Continuum and Distinct Element Numerical Modeling in Geomechanics, Itasca International, Shanghi, China, 2013.
[40] T. Van Steenkiste, J. van der Herten, I. Couckuyt, T. Dhaene, Data-Efficient Sensitivity Analysis with Surrogate Modeling, Uncertainty Modeling for Engineering Applications, Springer, 2019, pp. 55–69.